



**HAL**  
open science

## Characterization of rockfalls from seismic signal: insights from laboratory experiments

Maxime Farin, Anne Mangeney, Renaud Toussaint, Julien de Rosny, Nikolai Shapiro, Thomas Dewez, Clément Hibert, Christian Mathon, Olivier Sedan, Frédéric Berger

### ► To cite this version:

Maxime Farin, Anne Mangeney, Renaud Toussaint, Julien de Rosny, Nikolai Shapiro, et al.. Characterization of rockfalls from seismic signal: insights from laboratory experiments. *Journal of Geophysical Research*, 2015, 120 (10), pp.doi: 10.1002/2015JB012331. 10.1002/2015jb012331 . hal-01212961v2

**HAL Id: hal-01212961**

**<https://hal.science/hal-01212961v2>**

Submitted on 7 Oct 2015

**HAL** is a multi-disciplinary open access archive for the deposit and dissemination of scientific research documents, whether they are published or not. The documents may come from teaching and research institutions in France or abroad, or from public or private research centers.

L'archive ouverte pluridisciplinaire **HAL**, est destinée au dépôt et à la diffusion de documents scientifiques de niveau recherche, publiés ou non, émanant des établissements d'enseignement et de recherche français ou étrangers, des laboratoires publics ou privés.

# Characterization of rockfalls from seismic signal: insights from laboratory experiments

Maxime Farin,<sup>1</sup> Anne Mangeney,<sup>1,2</sup> Renaud Toussaint,<sup>3</sup> Julien de Rosny<sup>4</sup>,  
Nikolai Shapiro<sup>1</sup>, Thomas Dewez<sup>5</sup>, Clément Hibert<sup>6</sup>, Christian Mathon<sup>5</sup>,  
Olivier Sedan<sup>5</sup>, and Frédéric Berger<sup>7</sup>

---

Corresponding author: Maxime Farin, Seismology team, Institut de Physique du Globe de Paris, 1 rue Jussieu, 75238 Paris cedex 05, France. (farin@ipgp.fr)

<sup>1</sup>Institut de Physique du Globe de Paris,  
Sorbonne Paris Cité, CNRS (UMR 7154),  
Paris, France

<sup>2</sup>ANGE team, CEREMA, Inria, Lab.  
J.-L. Lions, CNRS, Paris, France

<sup>3</sup>IPGS-EOST, Géophysique  
Expérimentale, CNRS, Strasbourg, France

<sup>4</sup>Institut Langevin, Laboratoire Ondes et  
Acoustique, CNRS, Paris, France

<sup>5</sup>Service des Risques Naturels, BRGM,  
Orléans la Source, France

**Abstract.** The seismic signals generated by rockfalls can provide information on their dynamics and location. However, the lack of field observations makes it difficult to establish clear relationships between the characteristics of the signal and the source. In this study, scaling laws are derived from analytical impact models to relate the mass and the speed of an individual impactor to the radiated elastic energy and the frequency content of the emitted seismic signal. It appears that the radiated elastic energy and frequencies decrease when the impact is viscoelastic or elasto-plastic compared to the case of an elastic impact. The scaling laws are validated with laboratory experiments of impacts of beads and gravels on smooth thin plates and rough thick blocks. Regardless of the involved materials, the masses and speeds of the impactors are retrieved from seismic measurements within a factor of 3. A quantitative energy budget of the impacts is established. On smooth thin plates, the lost energy is either radiated in elastic waves or dissipated in viscoelasticity when the impactor is large or small with respect to the plate thickness, respectively. In contrast, on rough thick blocks, the elastic energy radiation represents less than 5% of the lost energy. Most of

---

<sup>6</sup>Lamont-Doherty Earth Observatory,

Palisades NY, US

<sup>7</sup>Unité de Recherche Ecosystèmes

Montagnards, Cemagref, Grenoble, France

the energy is lost in plastic deformation or rotation modes of the bead owing to surface roughness. Finally, we estimate the elastic energy radiated during field scale rockfalls experiments. This energy is shown to be proportional to the boulder mass, in agreement with the theoretical scaling laws.

## 1. Introduction

1 Rockfalls represent a major natural hazard in steep landscapes. Because of their unpre-  
2 dictable and spontaneous nature, the seismic monitoring of these gravitational instabili-  
3 ties has raised a growing interest for risks assessment in the last decades. Recent studies  
4 showed that rockfalls can be automatically detected and localized with high precision from  
5 the seismic signal they generate [*Suriñach et al.*, 2005; *Deparis et al.*, 2008; *Dammeier*  
6 *et al.*, 2011; *Hibert et al.*, 2011, 2014a]. A burning challenge is to obtain quantitative  
7 information on the gravitational event (volume, propagation velocity, extension,...) from  
8 the characteristics of the associated seismic signal [*Norris*, 1994; *Deparis et al.*, 2008; *Vila-*  
9 *josana et al.*, 2008; *Favreau et al.*, 2010; *Dammeier et al.*, 2011; *Hibert et al.*, 2011, 2014a;  
10 *Moretti et al.*, 2012, 2015; *Yamada et al.*, 2012].

11 Some authors found empirical relationships between the rockfall volume and the max-  
12 imum amplitude of the signal or the radiated seismic energy [*Norris*, 1994; *Hibert et al.*,  
13 2011; *Yamada et al.*, 2012]. The precursory work of *Norris* [1994] on rockfalls of large  
14 volume  $> 10^4 \text{ m}^3$  at Mount St Helens showed that the maximum amplitude of the emitted  
15 signal depends linearly on the rockfall volume. This is in agreement with the observa-  
16 tions of *Yamada et al.* [2012] on landslides triggered in Japan by Typhoon Talas in 2011.  
17 The authors observed that the integral of the squared signal amplitude measured at 1  
18 km from the source varied as the square the landslide volume. In contrast, *Hibert et al.*  
19 [2011] showed that the seismic energy emitted by rockfalls is proportional to their volume  
20 in the Dolomieu crater of the Piton de la Fournaise volcano, Réunion Island. Moreover,  
21 *Dammeier et al.* [2011] used a statistical approach and estimated the volume  $V$  of several

22 rockfalls in the central Alps from the measurement of the duration  $t_s$ , envelope area  
 23  $EA$  and peak amplitude  $PA$  of the generated seismic signal. For twenty well constrained  
 24 events, they found the empirical scaling law:  $V \propto t_s^{1.0368} EA^{-0.1248} PA^{1.1446}$ . The volumes  
 25 estimated with this relation were close to the measured ones but the results were sensitive  
 26 to the distance of the seismic stations from the events.

27 Other surveys investigated the ratio of the radiated seismic energy  $W_{el}$  over the potential  
 28 energy  $\Delta E_p$  lost by the rockfalls from initiation to deposition [*Deparis et al.*, 2008; *Hibert*  
 29 *et al.*, 2011, 2014a; *Lévy et al.*, 2015]. *Deparis et al.* [2008] studied ten rockfalls that  
 30 occurred between 1992 and 2001 in the french Alps and estimated that the ratio  $W_{el}/\Delta E_p$   
 31 was between  $10^{-5}$  and  $10^{-3}$ . *Hibert et al.* [2011, 2014a] observed that the ratios of the  
 32 seismic energy  $W_{el}$  radiated by the rockfalls in the Dolomieu crater over their potential  
 33 energy lost  $\Delta E_p$  varied from  $5 \cdot 10^{-5}$  to  $2 \cdot 10^{-3}$ . Finally, *Lévy et al.* [2015] found  $W_{el}/\Delta E_p \approx$   
 34  $1.1 \cdot 10^{-5} - 2.8 \cdot 10^{-5}$  for pyroclastic and debris flows that occurred on the Souffrière Hills  
 35 volcano in Montserrat Island, Lesser Antilles. Most of the aforementioned studies focused  
 36 on a specific rockfalls site [*Norris*, 1994; *Deparis et al.*, 2008; *Dammeier et al.*, 2011; *Hibert*  
 37 *et al.*, 2011, 2014a; *Yamada et al.*, 2012; *Lévy et al.*, 2015]. It is however difficult to test  
 38 the developed techniques on other sites because only a few of rockfalls areas are nowadays  
 39 simultaneously seismically and optically monitored.

40 Because gravitational events are very complex, it is still not clear what parameters  
 41 controls their seismic emission. The seismic signals generated by rockfalls on the field are  
 42 partially composed of waves emitted by individual impacts of boulders, triggering high  
 43 frequencies noise, typically higher than 1 Hz [e.g. *Deparis et al.*, 2008; *Vilajosana et al.*,  
 44 2008; *Helmstetter and Garambois*, 2010; *Hibert et al.*, 2014b; *Lévy et al.*, 2015] and by

45 long period stresses variations owing to the mass acceleration and deceleration over the  
46 topography, responsible for lower frequencies in the signal ( $< 1$  Hz) [e.g. *Kanamori and*  
47 *Given*, 1982; *Favreau et al.*, 2010; *Allstadt*, 2013]. To start the work on understanding the  
48 seismic emission of rockfalls, we focus here on the seismic signal generated by impacts.

49 The dynamics of impact can be described at first order by the classical model proposed  
50 by *Hertz* [1882] that gives the analytical expression of the force of impact of an elastic  
51 sphere on a solid elastic surface [see *Johnson*, 1985]. From the comparison of the impacts  
52 forces and durations measured from the emitted seismic signal with that predicted by *Hertz*  
53 [1882], *Buttle and Scruby* [1990] and *Buttle et al.* [1991] managed to retrieve the diameter  
54 of sub-millimetrical particles impacting a thick block. However, their computation was  
55 based on the direct compressive wave, measured at the opposite of the impact on the  
56 target block. Their configuration can therefore not be exported to field context. Also  
57 based on *Hertz* [1882]'s theory, *Tsai et al.* [2012] expressed the long period power spectral  
58 density generated by the impacts of sediments on the bed of rivers as a function of the  
59 river parameters such the particle size distribution, the impact rate and the bed load flux.  
60 From seismic measurements of *Burtin et al.* [2008] on trans-Himalayan Trisuli River, *Tsai*  
61 *et al.* [2012] were then able to quantitatively deduce the bed load flux.

62 In this paper, we adopt a similar approach. The basic idea is to derive from *Hertz*  
63 [1882]'s model analytical scaling laws relating the radiated elastic energy and the fre-  
64 quencies of the seismic signal generated by an impact to the mass and the speed of the  
65 impactor. These laws can then be inverted to deduce the impact parameters from a mea-  
66 surement of the emitted seismic signal. Note that *Tsai et al.* [2012] assumed for their  
67 analytical model that the impact duration was instantaneous because they focused on

68 signals of long periods compared with this duration. On the contrary, we do not assume  
69 an instantaneous impact here because we try here to use the whole spectrum content. In-  
70 deed, in order to robustly estimate the impact parameters from the emitted signal using  
71 our scaling laws, we need to determine the absolute energy radiated in elastic waves and,  
72 therefore, the entire amplitude spectrum of the seismic signal generated by the impact.  
73 This implies:

- 74 1. to record signal periods much smaller than the impact duration;
- 75 2. to know well the elastic properties of the impactor and of the substrate, i.e. their  
76 elastic moduli, their density, the type of mode excited in the substrate after an impact,  
77 its dispersion and how its energy attenuates with increasing distance from the source.

78 These two conditions are not easy to address in the field because usual sampling times  
79 are of the order of the typical impact durations ( $\sim 0.01$  s) and because of the strong  
80 heterogeneity of the ground. Therefore, in order to test our analytical scaling laws, we  
81 perform controlled laboratory experiments of impacts of spherical beads on thin plates  
82 with an ideal smooth surface, then on rough thick blocks i.e., in a context similar to that  
83 of the field. A series of impact experiments is also conducted with gravels to quantify  
84 how the relations between impacts properties and signal characteristics change when the  
85 impactor has a rough surface, which is a more realistic case i.e., closer to what is observed  
86 for natural rockfalls.

87 During an impact, a significant part of the impactor's energy can be lost in inelastic pro-  
88 cesses such as plastic i.e., irreversible, deformation of the impactor or the ground [Davies,  
89 1949] or viscoelastic dissipation in the vicinity of the impact [Falcon *et al.*, 1998]. These  
90 losses are not considered in *Hertz* [1882]'s elastic impact model. In this paper, we use



91 analytical models of viscoelastic and elasto-plastic impact to estimate how the frequen-  
92 cies of the emitted vibration and the radiated elastic energy deviate from that predicted  
93 using *Hertz* [1882]’s theory when inelastic dissipation occurs. Using these models, we  
94 interpret the discrepancy observed between the measured values in our experiments and  
95 those predicted by the elastic model of *Hertz* [1882]. Another advantage of the laboratory  
96 experiments is that the total energy lost during the impact can be easily measured from  
97 the velocity change of the impactor before and after the impact. We can then establish a  
98 quantitative energy budget among the energy radiated in elastic waves and that dissipated  
99 in inelastic processes. This allow us to better understand the process of wave generation  
100 by an impact and to roughly extrapolate what should be the relative importance of the  
101 different loss processes for natural rockfalls.

102 This paper is structured as follows. In section 2, we recall the theory for elastic, vis-  
103 coelastic and elasto-plastic impacts of a sphere on a plane surface and we derive the  
104 analytical scaling laws from this theory. The experimental setup is presented in section 3.  
105 In section 4, we test experimentally the scaling laws established in section 2 and retrieve  
106 the masses and speeds of the impactors from the measured seismic signals. In addition,  
107 we establish the energy budget of the impacts among elastic and inelastic losses and ob-  
108 serve how this budget varies on smooth thin plates and rough thick blocks when the bead  
109 mass and the elastic parameters change. In section 5, the discrepancy of the experimental  
110 results with the theory is discussed. Finally, the analytical scaling laws demonstrated in  
111 this paper are compared with empirical relations observed in drop experiments of large  
112 boulders in a natural context. We identify the issues that should be overcome in order to  
113 apply our scaling laws to natural impact situations.

## 2. Theory: Relations Between Impact Parameters and Seismic Characteristics

The vibration displacement  $\mathbf{u}(\mathbf{r}, t)$  at the distance  $\mathbf{r}$  from an impact is given by the time convolution of the force  $\mathbf{F}(\mathbf{r}_s, t)$  applied to the ground at position  $r_s$  with the Green's function  $\bar{\bar{\mathbf{G}}}(\mathbf{r}, \mathbf{r}_s, t)$  of the structure where the wave propagates [Aki and Richards, 1980]:

$$\mathbf{u}(\mathbf{r}, t) = \bar{\bar{\mathbf{G}}}(\mathbf{r}, \mathbf{r}_s, t) * \mathbf{F}(\mathbf{r}_s, t), \quad (1)$$

where  $*$  stands for the time convolution product. In our experiments, we only have access to the vibration acceleration in the direction normal to the surface  $a_z(r, t)$ . In the time Fourier domain, this acceleration is given by:

$$\tilde{A}_z(r, f) = -(2\pi f)^2 \tilde{G}_{zz}(r, f) \tilde{F}_z(f), \quad (2)$$

114 where  $f$  is the frequency and  $\tilde{F}_z(f)$  is the time Fourier transform of the vertical impact  
 115 force  $F_z(t)$ . The expression of the Green's function  $\tilde{G}_{zz}(r, f)$  is different when the impact  
 116 duration is greater or smaller than the two-way travel time of the emitted wave in the  
 117 structure thickness, i.e. for impacts on thin plates and on thick blocks, respectively. A  
 118 plate of thickness  $h$  vibrates normally to its surface because the fundamental  $A_0$  mode of  
 119 Lamb carries most of the energy [Royer and Dieulesaint, 2000; Farin et al., 2015]. The  
 120 module of the Green's function of this mode of vibration can be approximated by [e.g.  
 121 Goyder and White, 1980]:

$$122 \quad |\tilde{G}_{zz}(r, f)| = \frac{1}{8Bk^2} \sqrt{\frac{2}{\pi kr}}, \quad (3)$$

123 where  $k$  is the wave number,  $B = h^3 E_p / 12(1 - \nu_p^2)$  is the bending stiffness and  $E_p$  and  $\nu_p$   
 124 are the Young's modulus and the Poisson ratio of the impacted structure, respectively. At  
 125 low frequencies i.e., for  $kh \ll 1$ , the wave number  $k$  is related to the angular frequency  
 126  $\omega$  by  $k^4 = \omega^2 \rho_p h / B$ , where  $\rho_p$  is the plate density.

127 In contrast, an impact on a thick block generates compressive, shear and Rayleigh  
 128 waves [Miller and Pursey, 1955; Aki and Richards, 1980]. For  $kr \gg 1$  i.e., in far field,  
 129 the displacement mainly results from Rayleigh waves and the Green's function can be  
 130 approximated by [Miller and Pursey, 1955; Farin et al., 2015]:

$$131 \quad |\tilde{G}_{zz}(r, f)| \approx \frac{\xi^2 \omega}{2\mu c_P} \frac{\sqrt{x_0(x_0^2 - 1)}}{f_0'(x_0)} \sqrt{\frac{2c_P}{\pi \omega r}}, \quad (4)$$

132 where  $\mu$  is the shear Lamé coefficient,  $c_P$  is the compressional wave speed,  $\xi =$   
 133  $\sqrt{2(1 - \nu_p)/(1 - 2\nu_p)}$ ,  $f_0(x) = (2x^2 - \xi^2)^2 - 4x^2 \sqrt{(x^2 - 1)(x^2 - \xi^2)}$  and  $x_0$  is the real  
 134 root of  $f_0$ .

135 In this section, we derive analytical scaling laws that relate the energy radiated in  
 136 elastic waves and the characteristic frequencies of the vibration  $\tilde{A}_z(r, f)$  emitted by an  
 137 impact to the impact parameters (mass  $m$ , speed  $V_z$ ). Because the vibration  $\tilde{A}_z(r, f)$  is  
 138 controlled by the impact force  $\tilde{F}_z(f)$  [equation (2)], the scaling laws are different when  
 139 the impact is elastic or when viscoelastic dissipation or plastic deformation occur. Let  
 140 us first recall the expression of the impact force for an elastic impact and how it changes  
 141 for an inelastic impact. Note that we do not use any elasto-visco-plastic model of impact  
 142 here because elastic energy radiation, viscoelastic dissipation and plastic deformation are  
 143 never simultaneously significant in our experiments, even though it could be the case on  
 144 the field. For example, in certain cases, viscoelastic and plastic losses are negligible and  
 145 an elastic impact model is sufficient to describe the energy transfer.

## 2.1. Impact Models

### 146 2.1.1. Elastic Impact Model

#### 147 2.1.1.1. Hertz's Model

148 *Hertz* [1882] gives the force of elastic contact of a sphere of mass  $m$  on a plane as a  
 149 function of their interpenetration depth  $\delta_z(t)$  (Figure 1a):

$$150 \quad F_z(t) = -K\delta_z^{3/2}(t), \quad (5)$$

151 where

$$152 \quad K = \frac{4}{3}R^{1/2}E^*, \quad (6)$$

153 with  $R$ , the sphere radius and  $1/E^* = (1 - \nu_s^2)/E_s + (1 - \nu_p^2)/E_p$ , where  $\nu_s, \nu_p, E_s, E_p$  are  
 154 respectively the Poisson's ratios and the Young's moduli of the constitutive materials of  
 155 the sphere and the impacted plane.

156 During an impact, the displacement of the center of mass of the sphere is equal to the  
 157 interpenetration  $\delta_z(t)$ . Neglecting the gravity force, the equation of motion of the sphere  
 158 is then:

$$159 \quad m \frac{d^2\delta_z(t)}{dt^2} = -K\delta_z^{3/2}(t). \quad (7)$$

160 The solution of equation (7) is of the form  $\delta_z(t) = \delta_{z0}f(t/T_c)$ . The maximum interpenetration  
 161 depth  $\delta_{z0}$  and the impact duration  $T_c$  are respectively given by [*Johnson, 1985*]:

$$162 \quad \delta_{z0} = \left( \frac{5mV_z^2}{4K} \right)^{2/5}, \quad (8)$$

163 and

$$164 \quad T_c \approx 2.94 \frac{\delta_{z0}}{V_z} \approx 2.87 \left( \frac{16m^2}{9K^2V_z} \right)^{1/5}, \quad (9)$$

165 where  $V_z$  is the impact speed.

166 The maximum value of the impact force is therefore, according to equation (5):

$$167 \quad F_0 = K\delta_{z0}^{3/2} = K \left( \frac{5mV_z^2}{4K} \right)^{3/5}, \quad (10)$$

168 In the following, the interpenetration depth  $\delta_z(t)$ , the time  $t$  and the force  $F_z(t)$  are  
 169 respectively scaled by  $\delta_{z0}$ ,  $\delta_{z0}/V_z$  and  $F_0$ , that contain all the informations on the impact  
 170 characteristics.

### 171 2.1.1.2. Hertz-Zener's model for impacts on thin plates

172 *Hertz* [1882]'s model [equation (8)] is valid provided that the energy radiated in elastic  
 173 waves during the impact represents a small proportion of the impact energy  $\frac{1}{2}mV_z^{1/2}$   
 174 [*Hunter*, 1957; *Johnson*, 1985]. This is not the case when the thickness of the impacted  
 175 structure is around or lower than the diameter of the impactor, i.e. for impacts on thin  
 176 plates and membranes [e.g. *Zener*, 1941; *Farin et al.*, 2015]. When the energy lost in  
 177 plate vibration during the impact is not negligible, *Zener* [1941] proposed a more exact  
 178 description than *Hertz* [1882]'s model of the interaction between the sphere and the plate's  
 179 surface. One has to distinguish the sphere displacement  $z$ , given by:

$$180 \quad m \frac{d^2 z(t)}{dt^2} = -F_z(t), \quad (11)$$

181 from the plate's surface displacement  $u_z$  at the position of the impact, whose time deriva-  
 182 tive is:

$$183 \quad \frac{du_z(t)}{dt} = Y_{el} F_z(t), \quad (12)$$

184 where  $Y_{el}$  is the real part of the time derivative of the Green's function at the impact po-  
 185 sition  $\Re(dG_{zz}(r_0, t)/dt)$ , i.e. the radiation admittance. This function is given by [*Goyder*  
 186 *and White*, 1980] for plates:

$$187 \quad Y_{el} = \frac{1}{8\sqrt{B\rho_p h}}, \quad (13)$$

188 with  $B$ , the bending stiffness and  $h$ , the plate thickness. In these equations, the impact  
 189 force  $F_z(t)$  follows *Hertz* [1882]'s theory [equation (5)].

190 The difference of equation (11) and the derivative of equation (12) gives the following  
 191 equation for the relative movement of the sphere and of the substrate i.e., the interpenetration  
 192  $\delta_z(t) = z(t) - u_z(t)$ , in dimensionless form with  $\delta^* = \delta_z/\delta_{z0}$  and  $t^* = V_z t/\delta_{z0}$ :

193 
$$\frac{d^2\delta^*}{dt^{*2}} = -\frac{5}{4} \left( \delta^{*3/2} + \lambda_Z \frac{d\delta^*}{dt^*} \delta^{*1/2} \right), \quad (14)$$

194 with

195 
$$\lambda_Z \approx 0.175 \frac{E^{*2/5}}{\rho_s^{1/15} \sqrt{B\rho_p h}} m^{2/3} V_z^{1/5}. \quad (15)$$

196 In equation (14), we retrieve the impact model of *Hertz* [1882] [equation (7)] with  
 197 a corrective term that depends on the parameter  $\lambda_Z$ . This corrective term becomes  
 198 negligible when the thickness  $h$  of the structure is much larger than the diameter  $d$  of  
 199 the impactor because the parameter  $\lambda_Z$  tends towards 0 [Zener, 1941]. Therefore, for  
 200 impacts on elastic half-spaces i.e., on thick blocks, the corrective term disappears and the  
 201 model of *Zener* [1941] [equation (14)] matches with that of *Hertz* [1882] [equation (7)].  
 202 As a consequence, this model is only relevant for impacts on thin plates.

203 Equation (14) is solved numerically for different values of  $\lambda_Z$  with the initial conditions  
 204  $\delta^*(0) = 0$  and  $\frac{d\delta^*}{dt^*}(0) = 1$ . The impact force  $F_z(t)/F_0 = \delta^{*3/2}$  is shown on Figure 1b.  
 205 When  $\lambda_Z$  increases i.e., when  $m$  and  $V_z$  increase, the force profile loses its symmetry  
 206 with respect to its maximum, its amplitude decreases and its duration increases. For an  
 207 inelastic coefficient  $\lambda_Z = 0.25$ , the force is only slightly affected. Practically,  $\lambda_Z$  is always  
 208 smaller than 0.5 in our experiments.

209 **2.1.2. Viscoelastic Impact Model**

210 Viscoelastic dissipation is related to the viscosities of the materials involved in the  
 211 impact and can be described as a heat loss. Viscoelastic solids are often represented by

212 a spring and a dashpot in parallel (Kelvin-Voigt model). *Hertz* [1882]'s theory has been  
 213 extended to viscoelastic impacts, adding a force  $F_{diss}(t)$  in equation (7) to model viscous  
 214 dissipation [*Kuwabara and Kono*, 1987; *Falcon et al.*, 1998; *Ramírez et al.*, 1999]:

$$215 \quad F_{diss}(t) = -\frac{3}{2}DK \frac{d\delta_z(t)}{dt} \delta_z^{1/2}(t), \quad (16)$$

216 with  $D$ , a characteristic time depending on the materials viscosities and elastic constants  
 217 [*Hertzsch et al.*, 1995; *Brilliantov et al.*, 1996; *Ramírez et al.*, 1999]. The expression of  $D$   
 218 is only given in the literature in case when the sphere and the plane have the same elastic  
 219 parameters  $E$  and  $\nu$ :

$$220 \quad D = \frac{2}{3} \frac{\chi^2}{(\chi + 2\eta)} \frac{(1 - \nu^2)(1 - 2\nu)}{E\nu^2}, \quad (17)$$

221 where  $\chi$  and  $\eta$  are the bulk and shear viscosities, respectively. We can not measure these  
 222 two last parameters in our experiments and they are not tabulated in our frequencies  
 223 range of interest, therefore  $D$  will be an adjustable parameter.

224 The dimensionless equation of motion for a viscoelastic impact is then:

$$225 \quad \frac{d^2\delta^*}{dt^{*2}} = -\frac{5}{4} \left( \delta^{*3/2} + \alpha \frac{d\delta^*}{dt^*} \delta^{*1/2} \right), \quad (18)$$

226 which is the same expression as for *Zener* [1941]'s model [equation (14)] but with a  
 227 different parameter:

$$228 \quad \alpha = \frac{3}{2} D \frac{V_z}{\delta_{z0}} \simeq 1.4 D \frac{E^{*2/5} V_z^{1/5}}{\rho_s^{1/15} m^{1/3}}, \quad (19)$$

229 the viscoelastic parameter [*Ramírez et al.*, 1999]. For  $\alpha = 0$  (i.e.,  $D = 0$ ), equation (18)  
 230 matches with equation (7) for elastic impacts.

231 Because equations (14) and (18) are identical, when  $\alpha$  increases the force profile varies  
 232 exactly the same way as when  $\lambda_z$  increases in *Zener* [1941]'s model (Figure 1b). However,

233 note that the corrective terms to *Hertz* [1882]’s model in the viscoelastic and *Zener* [1941]’s  
 234 models have a different physical origin. The viscoelastic corrective term is due to the fact  
 235 that the impactor and the ground have an intrinsic viscosity [*Falcon et al.*, 1998]. This  
 236 term is stronger when the mass  $m$ , or diameter  $d$ , of the sphere decreases [equation (19)].  
 237 On the contrary, the corrective term of *Zener* [1941]’s model comes from the fact that a  
 238 larger amount of the impactor’s kinetic energy is transferred into plate vibration during  
 239 the impact when the sphere’s diameter  $d$  is large compared to the plate thickness  $h$  [*Zener*,  
 240 1941] [equation (15)]. We can therefore assume that the viscoelastic and *Zener* [1941]’s  
 241 impact models are never simultaneously effective.

### 242 2.1.3. Elasto-plastic Impact Model

243 Plastic (i.e. not reversible) deformations result from irreversible structural modifications  
 244 which occur when the pressure on the contact area  $P(t) = F_z(t)/2\pi R\delta_z(t)$  reaches the  
 245 dynamic yield strength  $P_Y = 3Y_d$  of the material, where  $Y_d$  is the dynamic yield stress of  
 246 the softest material [*Crook*, 1952; *Johnson*, 1985]. Plastic deformation can be evidenced  
 247 by the apparition of a crater at the impact position. The energy lost to create this crater  
 248 modifies the shape of the impact force with respect to the case of an elastic or viscoelastic  
 249 impact. A model was proposed by *Troccaz et al.* [2000] to describe the evolution of the  
 250 impact force when the limit of elastic behavior is exceeded. This model is based on the  
 251 hypothesis that only the sphere or the structure deforms plastically. Such an impact is  
 252 composed of three successive phases:

- 253 1. The impact is elastic while  $P(t) < P_Y$  and the impact force  $F(t)$  follows equation  
 254 (5);



255 2. When  $P(t) \geq P_Y$  the deformation is fully plastic and the force expression becomes  
 256  $F_z(t) = -2\pi R P_Y \delta_z(t)$  until the force reaches a maximum  $F_{max}$ , which is smaller than the  
 257 maximum value  $F_0$  for an elastic impact;

258 3. The rebound is elastic with  $F_z(t) = F_{max} ((\delta_z(t) - \delta_r)/(\delta_{max} - \delta_r))^{3/2}$ , where  $\delta_{max}$   
 259 is the maximum interpenetration reached and  $\delta_r$  is the residual deformation after plastic  
 260 deformation, that is neglected (i.e., considered to be 0) in the following.

261 The dimensionless equation of motion during plastic deformation (phase 2) is then, if  
 262  $\delta_z(t)$  and time  $t$  are respectively scaled by  $\delta_{z0}$  and  $\delta_{z0}/V_z$ :

$$263 \quad \frac{d^2\delta^*}{dt^{*2}} = -\frac{5}{4} \frac{P_Y}{P_0} \delta^*, \quad (20)$$

264 where  $P_0$  is the maximum stress during Hertz's elastic impact:

$$265 \quad P_0 = \frac{K\delta_{z0}^{3/2}}{2\pi R\delta_{z0}} = \frac{2}{3\pi} \left(\frac{5}{4}\right)^{1/5} \rho_s^{1/5} E^{*4/5} V_z^{2/5}. \quad (21)$$

266 Equation (20) depends only on the stresses ratio  $P_Y/P_0$  that is independent of the  
 267 impactor mass  $m$ . When this ratio is greater or equal to 1, the impact is purely elastic.  
 268 The amplitude of the impact force decreases as the stresses ratio  $P_Y/P_0$  decreases (Figure  
 269 1c). Both the duration of the impact and the time to reach the maximum amplitude  
 270 increase for an elasto-plastic impact with respect to the elastic case.

## 2.2. Analytical Scaling Laws

271 The seismic signal generated by an impact can be characterized by the radiated elastic  
 272 energy  $W_{el}$  and by a frequency. Here we relate analytically these seismic characteristics  
 273 with the mass  $m$  and the speed  $V_z$  of the impactor using the impact models presented  
 274 above.

### 2.2.1. Radiated Elastic Energy

276 The energy  $W_{el}$  radiated in elastic waves is the work done by the impact force  $F_z(t)$   
 277 during the impact, i.e.,

$$278 \quad W_{el} \hat{=} \int_{-\infty}^{+\infty} F_z(t) \frac{du_z(t)}{dt} dt = \int_{-\infty}^{+\infty} |\tilde{F}_z(f)|^2 \tilde{Y}_{el}(f) df, \quad (22)$$

279 according to Parseval's theorem, where  $\frac{du_z(t)}{dt}$  is the vibration speed at the impact position  
 280 [equation (12)] and  $\tilde{Y}_{el}(f)$  is the time Fourier transform of the radiation admittance.

281 The radiated elastic energy  $W_{el}$  is different for impacts on thin plates and on thick blocks  
 282 because the radiation admittance  $\tilde{Y}_{el}(f)$  has a different expression. Developing equation  
 283 (22), we obtain in Table 1 analytical expressions for the elastic energy  $W_{el}$  radiated during  
 284 an impact on thin plates and thick blocks, as a function of the impact parameters (see  
 285 Appendix A for details on the calculations). On thin plates,

$$286 \quad W_{el} = a_1 C_{plate} m^{5/3} V_z^{11/5} \quad (23)$$

287 and, on thick blocks,

$$288 \quad W_{el} = a_2 C_{block} m V_z^{13/5}, \quad (24)$$

289 where coefficients  $a_1$  and  $a_2$  depends only on the elastic parameters (see Table 1). In these  
 290 expressions,  $C_{plate} = \int_{-\infty}^{+\infty} |g(t^*)|^2 dt^*$  and  $C_{block} = \int_0^{+\infty} f^{*2} |\tilde{g}(f^*)|^2 df^*$ , where  $|g(t^*)| =$   
 291  $|F_z(t)|/F_0$  with  $t^* = V_z t / \delta_{z0}$  and where  $\tilde{g}(f^*)$  is the time Fourier transform of  $g(t^*)$ . For  
 292 an elastic impact i.e., with  $F_z(t)$  given by equation (5), we obtain  $C_{plate} \simeq 1.21$  and  $C_{block} \simeq$   
 293  $0.02$ . The function  $g(t^*)$  has a lower amplitude when the impact is inelastic compared to  
 294 the case of an elastic impact (Figures 1b and 1c). Therefore, both coefficients  $C_{plate}$  and  
 295  $C_{block}$  decrease when the viscoelastic parameter  $\alpha$  increases and when the stresses ratio  
 296  $P_Y/P_0$  decreases (Figures 2a and 2b). Moreover, on thin plates  $C_{plate}$  also decreases when  
 297 the parameter  $\lambda_Z$  increases (Figure 2a). As a consequence, less energy is radiated in the

298 form of elastic waves when the impact is inelastic with respect to the case of an elastic  
 299 impact.

300 On thick blocks, the radiated elastic energy  $W_{el}$  is proportional to the impactor's mass  
 301  $m$  for a given impact speed  $V_z$  [equation (24)]. Moreover, the ratio of  $W_{el}$  over the impact  
 302 energy  $E_c = \frac{1}{2}mV_z^2$  varies as  $V_z^{3/5}$  and is independent of the sphere mass  $m$ , which is in  
 303 agreement with *Hunter* [1957]'s findings.

304 It is important to note that the analytical expressions for the radiated elastic energy  $W_{el}$   
 305 in Table 1 are only controlled by the impact force  $F_z$  and by the rheological parameters of  
 306 the impactor and the substrate in the vicinity of the impact but do not depend on wave  
 307 dispersion and viscous dissipation during wave propagation within the substrate.

### 308 2.2.2. Characteristic Frequencies

309 The frequency content of the seismic signal emitted by an impact can give information  
 310 on the impact duration. To describe the amplitude spectrum  $|\tilde{A}_z(r, f)|$  of the acceleration  
 311 vibration, we can either measure:

312 1. A mean frequency  $f_{mean}$  that is less sensitive to the signal to noise ratio than the  
 313 frequency for which the amplitude spectrum is maximum [*Vinningland et al.*, 2007a, b]:

$$314 \quad f_{mean} = \frac{\int_0^{+\infty} |\tilde{A}_z(r, f)| f df}{\int_0^{+\infty} |\tilde{A}_z(r, f)| df}, \quad (25)$$

315 2. The bandwidth  $\Delta f$ :

$$316 \quad \Delta f = 2 \sqrt{\frac{\int_0^{+\infty} |\tilde{A}_z(r, f)| f^2 df}{\int_0^{+\infty} |\tilde{A}_z(r, f)| df} - f_{mean}^2}. \quad (26)$$

317 Regardless of the complexity (fracturation, layers, ...) of the substrate where the waves  
 318 emitted by the impact propagate, it is important to notice that the mean frequency  
 319  $f_{mean}$  and the bandwidth  $\Delta f$  are always inversely proportional to the duration of the

320 impact, which is given by the force history at the position of the impact. Here, we  
 321 normalize these frequencies by *Hertz* [1882]’s impact duration  $T_c$ . The coefficients of  
 322 proportionality between  $f_{mean}$ ,  $\Delta f$  and  $1/T_c$  are estimated for elastic, viscoelastic and  
 323 elasto-plastic impacts by computing a synthetic spectrum  $|\tilde{A}_z(r, f)|$  using equation (2)  
 324 with the forces represented in Figures 1b and 1c for different values of  $\alpha$  and  $P_Y/P_0$ . The  
 325 frequencies for an elastic impact i.e., for  $\alpha = 0$  and  $P_Y/P_0 = 1$ , are given in Table 2. Both  
 326 frequencies  $f_{mean}$  and  $\Delta f$  are smaller when the impact is inelastic compared to the case  
 327 of an elastic impact (Figure 3). They decrease by  $\sim 5\%$  when  $\alpha$  increases from 0 to 0.5  
 328 and by  $\sim 25\%$  when the stresses ratio  $P_Y/P_0$  decreases from 1 to 0.5.

329 When normalized by  $T_c$ , the characteristic frequencies are also affected by wave disper-  
 330 sion and viscous attenuation of energy during propagation i.e. by the Green’s function of  
 331 the structure. These propagation effects are independent of the profile of the impact force,  
 332 i.e. of the fact that the impact is elastic or inelastic. For the computation of the charac-  
 333 teristic frequencies on thick blocks, we used for simplicity the far field approximation of  
 334 the Green’s function of Rayleigh waves [equation (4)]. This approximation is correct for  
 335 impacts on homogeneous media such that investigated in the laboratory experiments of  
 336 section 4. In the field, however, the propagation medium is much more complex and other  
 337 modes with a different dispersion could develop. In this case, the frequencies normalized  
 338 by  $T_c$  shown in Table 2 could change. Active or passive seismic surveys can allow to eval-  
 339 uate locally the Green’s function of a specific site. This Green’s function can then be used  
 340 in equations (25) and (26) to estimate how much the normalized frequencies divert from  
 341 that computed using the Green’s function of Rayleigh waves. This is however beyond the  
 342 scope of the paper. In addition to dispersion, viscous attenuation of energy during prop-

343 agation can have a significant influence on the measured frequency on the field, especially  
344 for high frequencies. [Gimbert *et al.*, 2014] investigated the amplitude spectrum gener-  
345 ated by the turbulent flow in rivers and showed that its central frequency can decrease  
346 by a factor of 10 when the distance  $r$  from the source increases from 5 m to 600 m, for  
347 a quality factor  $Q = 20$ . To quantify the effect of viscous attenuation on frequencies in  
348 our impact experiments, we multiply the synthetic spectrum in equations (25) and (26)  
349 by the factor  $\exp(-\gamma(\omega)r)$ , where  $1/\gamma(\omega)$  represents the characteristic distance of energy  
350 attenuation. In our experiments, the propagation media are homogeneous and we record  
351 the seismic signals close to the impacts, from  $r = 2$  cm to about  $r = 30$  cm. In this range  
352 of distances  $r$  and for the substrates investigated in section 4, we estimate that the char-  
353 acteristic frequencies  $f_{mean}$  decreases and  $\Delta f$  increases by less than 5% when  $r$  increases,  
354 which is negligible. However, for every practical applications, it is crucial to evaluate wave  
355 dispersion and viscous attenuation during propagation and correct the measured seismic  
356 signal from these effects before computing its energy  $W_{el}$  and its frequencies  $f_{mean}$  and  
357  $\Delta f$ . This correction is systematically performed in our experiments.

### 358 2.2.3. Inverse Scaling Laws

359 We can invert the scaling laws derived in this section for the radiated elastic energy  
360  $W_{el}$  and for the frequencies  $f_{mean}$  and  $\Delta f$  (Tables 1 and 2) to express the mass  $m$  and  
361 the impact speed  $V_z$  as functions of the radiated elastic energy  $W_{el}$  and a characteristic  
362 frequency  $f_c$  of the seismic signal that is either  $f_{mean}$  or  $\Delta f$ .

363 On thin plates,  $W_{el} = a_1 C_{plate} m^{5/3} V_z^{11/5}$ ,  $f_{mean} = 0.75/T_c$  and  $\Delta f = 0.72/T_c$ , then,  
 364 developing the expression of  $T_c$  [equation (9)], we obtain:

$$365 \quad m = c_1 \left( \frac{E^{*2}}{(a_1 C_{plate})^{3/11} \rho_s^{1/3}} \right)^{11/16} \frac{W_{el}^{3/16}}{f_c^{33/16}} \quad (27)$$

366 and

$$367 \quad V_z = c_2 \left( \frac{\rho_s^{1/3}}{a_1 C_{plate} E^{*2}} \right)^{5/16} W_{el}^{5/16} f_c^{25/16}, \quad (28)$$

368 where  $c_1 \approx 0.046$  or  $0.05$  and  $c_2 \approx 10.8$  or  $10.1$  if  $f_c$  is  $f_{mean}$  or  $\Delta f$ , respectively. The  
 369 coefficient  $a_1$  is given in Table 1.

370 On thick blocks, the inversion of the relations  $W_{el} = a_2 C_{block} m V_z^{13/5}$ ,  $f_{mean} = 1/T_c$  and  
 371  $\Delta f = 0.6/T_c$  gives:

$$372 \quad m = c_3 \left( \frac{E^{*6/5}}{(a_2 C_{block})^{3/13} \rho_s^{1/5}} \right)^{13/16} \frac{W_{el}^{3/16}}{f_c^{39/16}} \quad (29)$$

373 and

$$374 \quad V_z = c_4 \left( \frac{\rho_s^{1/5}}{a_2 C_{block} E^{*6/5}} \right)^{5/16} W_{el}^{5/16} f_c^{15/16}, \quad (30)$$

375 where  $c_3 \approx 4.88$  or  $4.7$  and  $c_4 \approx 0.018$  or  $0.02$  if  $f_c$  is  $f_{mean}$  or  $\Delta f$ , respectively. The value  
 376 of  $a_2$  is given in Table 1.

377 The physical characteristics of an impact can then be theoretically deduced from the  
 378 generated seismic signal. With a continuous recording the seismic signals emitted by  
 379 rockfalls, such that performed in Dolomieu crater, Réunion Island [e.g. *Hibert et al.*,  
 380 2014a], the relations (27) to (30) could be very useful for risks assessment related to these  
 381 events. Note that the estimation of the impact parameters  $m$  and  $V_z$  requires a prior  
 382 evaluation of the elastic properties  $\rho_i$ ,  $E_i$  and  $\nu_i$  of the impactor and the ground. It  
 383 should also be noticed that  $m$  and  $V_z$  strongly depend on the frequency  $f_c$ . For example

384 on blocks, if the characteristic frequency is underestimated by a factor of 2, the mass  
 385  $m$  will be overestimated by a factor of  $2^{39/16} \simeq 5.4$ . It is therefore necessary to record  
 386 the entire frequency spectrum to obtain a good estimation of the impact parameters.  
 387 Because of temporal aliasing during signal sampling, an ideal sampling frequency should  
 388 be higher than two times the highest frequency of the spectrum, that should be at least  
 389  $f_{mean} + \Delta f/2$ . According to Table 2, the sampling frequency should then be at minimum  
 390  $3/T_c$ .

391 In section 4.3, the scaling laws presented in Tables 1 and 2 are tested with impacts ex-  
 392 periments. Moreover, the masses  $m$  and the speeds  $V_z$  of the impactors in the experiments  
 393 are retrieved from the measured seismic signals using equations (27) to (30) and they are  
 394 compared with their real values.

### 2.3. Energy Budget and Coefficient of Restitution

395 Another objective of this paper is to establish an energy budget of the impacts. To  
 396 that way, we compare the radiated elastic energy  $W_{el}$  to the total energy lost during the  
 397 impact  $\Delta E_c$ . From a practical point of view, the total energy lost by a spherical bead  
 398 rebounding normally and without rotation can be easily measured from the difference of  
 399 the bead kinetic energy before and after the impact:

$$400 \quad \Delta E_c = \frac{1}{2}mV_z^2(1 - e^2), \quad (31)$$

401 where  $e$  is the normal coefficient of restitution, that is the ratio of the bead vertical speeds  
 402 after and before the impact, respectively  $V'$  and  $V_z$  [e.g. *Tillet*, 1954; *Hunter*, 1957; *Reed*,  
 403 1985; *Falcon et al.*, 1998; *McLaskey and Glaser*, 2010].

404  $\Delta E_c$  is the sum of the energy radiated in elastic waves ( $W_{el}$ ), lost in viscoelastic dissi-  
 405 pation in the vicinity of the contact ( $W_{visc}$ ) and dissipated by all other processes ( $W_{other}$ ).  
 406 These other losses can be due to plastic deformation [Davies, 1949], surface forces between  
 407 the sphere and the surface, as e.g. electrostatic forces [Israelachvili, 2002], or in general  
 408 grain scale interactions [Duran, 2010; Andreotti et al., 2013]:

$$409 \quad \Delta E_c = W_{el} + W_{visc} + W_{other}. \quad (32)$$

410 In our impacts experiments, the radiated elastic energy  $W_{el}$  is deduced from a mea-  
 411 surement of the generated seismic signal. Here we present an analytical expression for  
 412 the energy  $W_{visc}$  that will be used later to estimate the losses related to viscoelastic  
 413 dissipation.

### 414 2.3.1. Energy Lost by Viscoelastic Dissipation

415 The energy  $W_{visc}$  lost by viscoelastic dissipation in the vicinity of the impact results  
 416 from the work done by the viscoelastic force  $F_{diss} = -\frac{3}{2}DK \frac{d\delta_z(t)}{dt} \delta_z^{1/2}(t)$  during the impact:

$$417 \quad W_{visc} = \int_0^{+\infty} F_{diss}(t) \cdot \frac{d\delta_z(t)}{dt} dt. \quad (33)$$

418 Using the dimensionless variables  $\delta^* = \delta_z/\delta_{z0}$  and  $t^* = V_z t/\delta_{z0}$  and the viscoelastic pa-  
 419 rameter  $\alpha = \frac{3}{2}DV_z/\delta_{z0}$ , we can show that:

$$420 \quad W_{visc} = C_{visc} m V_z^2, \quad (34)$$

421 where  $C_{visc} = \int_0^{+\infty} \left(\frac{d\delta^*}{dt^*}\right)^2 \delta^{*1/2} dt^*$  is a function of  $\alpha$  only (Figure 2c). For an elastic  
 422 impact, no work is done by the viscoelastic force because  $C_{visc} = 0$ . The expression of  
 423  $W_{visc}$  is independent of the fact that the impact is on a plate or on a block because it  
 424 concerns the energy dissipated in the impact region.



425 The proportion of total energy  $E_c$  dissipated by viscoelasticity can be developed in  
 426 powers of the mass  $m$  and the impact speed  $V_z$  using the third order Taylor series  $C_{visc} \approx$   
 427  $1.24\alpha - 1.51\alpha^2 + 0.86\alpha^3$  and the expression of  $\alpha$  in equation (19):

$$428 \quad \frac{W_{visc}}{E_c} = 2C_{visc} \approx 3.47x - 5.92x^2 + 4.72x^3 + O(x^3), \quad (35)$$

429 where  $x = DE^{*2/5}\rho_s^{-1/15}m^{-1/3}V_z^{1/5}$ , which is in agreement with the viscoelastic impact  
 430 models of *Kuwabara and Kono* [1987] and *Ramírez et al.* [1999].

### 431 2.3.2. Total Energy Lost

432 Finally, if we assume that the sole energy dissipation processes are elastic waves radia-  
 433 tion and viscoelastic dissipation and that other energy dissipation processes (e.g. plastic  
 434 deformation) are negligible, the proportion of the lost energy  $\Delta E_c$  radiated in elastic waves  
 435 is, on plates:

$$436 \quad \frac{W_{el}}{\Delta E_c} = \frac{a_1 C_{plate} m^{2/3} V_z^{1/5}}{a_1 C_{plate} m^{2/3} V_z^{1/5} + C_{visc}}, \quad (36)$$

437 and the proportion of the lost energy  $\Delta E_c$  dissipated in viscoelasticity is:

$$438 \quad \frac{W_{visc}}{\Delta E_c} = \frac{C_{visc}}{a_1 C_{plate} m^{2/3} V_z^{1/5} + C_{visc}}. \quad (37)$$

439 In these expressions, at first order  $C_{visc} \propto m^{-1/3}$  [equation (35)]. Therefore, when the  
 440 mass  $m$  of the impactor increases, the proportion of the lost energy  $\Delta E_c$  radiated in  
 441 elastic waves should tends towards 100% and that lost by viscoelastic dissipation should  
 442 tends toward 0%. The transition from a viscoelastic impact (for small masses) towards an  
 443 elastic impact (for large masses) occurs when  $a_1 C_{plate} m^{2/3} V_z^{1/5} = C_{visc}$ , i.e. for a critical  
 444 mass  $m_c \approx 8D\sqrt{B\rho_p h}$ .

445 On blocks, we get:

$$446 \quad \frac{W_{el}}{\Delta E_c} = \frac{a_2 C_{block} V_z^{3/5}}{a_2 C_{block} V_z^{3/5} + C_{visc}}, \quad (38)$$

447 and

$$448 \quad \frac{W_{visc}}{\Delta E_c} = \frac{C_{visc}}{a_2 C_{block} V_z^{3/5} + C_{visc}}. \quad (39)$$

449 For large masses  $m$ , the ratio  $W_{el}/\Delta E_c$  becomes independent of  $m$  and tends towards  
 450 100% because  $C_{visc}$  is negligible. When  $m$  decreases, the ratio  $W_{el}/\Delta E_c$  decreases and the  
 451 ratio  $W_{visc}/\Delta E_c$  increases.

452 This model is somewhat ideal because the energy dissipated by other processes such as  
 453 plastic deformation are not negligible when the impactor's mass  $m$  is large, in particular  
 454 when the contact surface is rough. As a consequence, the ratio  $W_{el}/\Delta E_c$  practically never  
 455 reaches 100% when  $m$  increases (see section 4.4.2).

456 The validity of theoretical scaling laws established in this section for the radiated elastic  
 457 energy, the frequencies and the lost energy is tested in section 4 with simple impact  
 458 experiments. Prior to this, the experimental setup is presented in the next section.

### 3. Experimental Setup

459 We conduct laboratory experiments of beads and gravels impacts on horizontal hard  
 460 substrates. The generated seismic vibration is recorded on the surface by mono-component  
 461 piezoelectric charge shock accelerometers (type 8309, *Brüel & Kjaer*). The response of  
 462 the sensors is flat between 1 Hz and 54 kHz. The impactor is initially held by a screw  
 463 and dropped without initial velocity and rotation to ensure reproducibility (Figure 4a).  
 464 The height of fall  $H$  varies between 2 cm and 40 cm. The impact speed  $V_z$  is calculated  
 465 assuming a fall without air friction:  $V_z = \sqrt{2gH}$ , with  $g$  the gravitational acceleration.

466 We drop spherical beads of steel, glass and polyamide (Figure 4b) of diameter  $d$  ranging  
467 from 1 mm to 20 mm to observe the influence of the mass and of the elastic parameters on  
468 the results. We conduct the same experiments with granite gravels of irregular shapes and  
469 of similar size and mass than the beads to test if the analytical scaling laws established  
470 for spheres impacts are still valid if the impactor is not spherical. The properties of the  
471 impactors used in the experiments are shown in Table 3.

472 Four target substrates are used: (i) a smooth PMMA plate of dimensions  $120 \times 100 \times 1$   
473  $\text{cm}^3$ , (ii) a circular 1 cm-thick smooth glass plate of radius 40 cm, (iii) a rough marble block  
474 of dimensions  $20 \times 20 \times 15 \text{ cm}^3$  and (iv) a rough concrete pillar of dimensions  $3 \times 1.5 \times 0.6$   
475  $\text{m}^3$ . The seismic vibration is recorded at different distances from the impacts to measure  
476 waves group speed  $v_g = \partial\omega/\partial k$  and phase speed  $v_\phi = \omega/k$  of the direct wave front in these  
477 substrates. These characteristics and the elastic parameters of the investigated structures  
478 are summarized in Table 4. Note that we assume that the rheological properties  $E_p$ ,  $\nu_p$   
479 and  $\rho_p$  of the substrates at the position of the impact are the same than that within  
480 the substrates, where the waves propagate. This hypothesis is valid for the homogeneous  
481 solids investigated here but it may not be correct in the fractured and layered media  
482 encountered in the field, whose elastic properties vary with depth. In any cases, it is  
483 necessary to determine these properties in order to quantify the radiated elastic energy  
484  $W_{el}$  and to deduce thereafter the impact parameters  $m$  and  $V_z$  from the seismic signal.

## 4. Experimental Results

### 4.1. Methods to Estimate the Radiated Elastic Energy

485 Let us first describe the signals recorded in our experiments of bead impacts on the  
486 different substrates and how we compute the radiated elastic energy  $W_{el}$  in each case.

487 A bouncing bead generates a series of short and impulsive acoustic signals (Figures 5a,  
 488 5b, 6a and 6b). The bead can rebound more than 50 times on the smooth glass plate  
 489 while it rebounds only 2 or 3 times on the concrete block owing to surface roughness  
 490 (Figures 5b and 6a). We estimate the coefficient of normal restitution  $e = \sqrt{H'/H}$  from  
 491 the time of flight  $\Delta t$  between the successive rebounds because the rebound height is given  
 492 by  $H' = g\Delta t^2/8$  [Falcon et al., 1998; Farin, 2015]. The total energy lost during an impact  
 493 is then given by  $1 - e^2$  [see equation (31)].

494 The PMMA and glass plates and the concrete block are sufficiently large to measure  
 495 most of the first wave arrival before the return of the first reflections off the lateral sides  
 496 (Figures 5c, 5f and 6e). In these cases, we estimate the radiated elastic energy  $W_{el}$  from  
 497 the energy flux crossing a surface surrounding the impact, as detailed in Farin et al. [2015]  
 498 i.e., for plates:

$$499 \quad W_{el} = 2rh\rho_p \int_0^{+\infty} v_g(\omega) |\tilde{V}_z(r, \omega)|^2 \exp(\gamma(\omega)r) d\omega, \quad (40)$$

500 and for blocks:

$$501 \quad W_{el} = 2\rho_p r v_g c_P \pi_R^{surf}(r) \frac{\beta(f'_0(x_0))^2}{2\pi\xi^4(x_0^2 - 1)} \int_0^{+\infty} |\tilde{V}_z(r, \omega)|^2 \omega^{-1} \exp(\gamma(\omega)r) d\omega. \quad (41)$$

502 In these expressions,  $v_g$  is the group speed,  $|\tilde{V}_z(r, \omega)|$  is the time Fourier transform of  
 503 the vertical vibration speed at the surface and  $\pi_R^{surf}(r)$  is the percentage of Rayleigh  
 504 waves in the signal at the surface at distance  $r$  from the impact [Farin et al., 2015]. The  
 505 factor  $\exp(\gamma(\omega)r)$  compensates viscoelastic dissipation with distance. The characteristic  
 506 distance of energy attenuation  $1/\gamma(\omega)$  is estimated experimentally for every substrates  
 507 (Table 4) [see Farin et al., 2015, for details]. The coefficient  $\beta$  depends only on the  
 508 Poisson's ratio  $\nu_p$  (see Figure 17 in Appendix A).

509 Because the substrates size is limited, wave reflections off the boundaries are recorded by  
 510 the sensors. Side reflections are strongly attenuated in PMMA which is a more damping  
 511 material than glass, concrete and marble (Figure 5c). On contrary, the wave is reflected  
 512 many times in the glass plate and in the two blocks and its averaged amplitude decreases  
 513 exponentially with time owing to viscous dissipation during wave propagation (Figures 5d,  
 514 6c and 6d). An adjustment of an exponential curve on the squared signal, filtered below  
 515 2000 Hz, allows us to quantify the characteristic decay time of energy  $\tau$  in the substrate  
 516 (Table 4) [see Appendix B of *Farin et al.*, 2015, for details on the experimental procedure].  
 517 This situation is referred to as a diffuse field in the literature [e.g. *Weaver*, 1985; *Mayeda*  
 518 *and Malagnini*, 2010; *Sánchez-Sesma et al.*, 2011]. In this case, we can estimate the  
 519 radiated elastic energy  $W_{el}$  from the reflected coda. Indeed, in diffuse field approximation,  
 520 the squared normal vibration speed averaged over several periods decreases exponentially:

$$521 \quad \overline{v_z(t)^2} = \overline{v_z(t=0)^2} \exp\left(-\frac{t}{\tau}\right), \quad (42)$$

522 where  $t = 0$  is the instant of the impact. Knowing the characteristic time  $\tau$ , we extrapolate  
 523 the vibration speed at the instant  $t = 0$  and deduce the radiated elastic energy  $W_{el}$  from  
 524 [*Farin et al.*, 2015]:

$$525 \quad W_{el} \approx \left(1 + \left(\frac{\mathcal{H}}{\mathcal{V}}\right)_{\text{diffuse}}^2\right) \rho_p V \overline{v_z(t=0)^2}, \quad (43)$$

526 where  $V$  is the block volume and  $\left(\frac{\mathcal{H}}{\mathcal{V}}\right)_{\text{diffuse}}$  is the ratio of horizontal to vertical amplitude  
 527 at the surface of the structure in diffuse field approximation. On thin plates,  $\left(\frac{\mathcal{H}}{\mathcal{V}}\right)_{\text{diffuse}} \simeq 0$ .  
 528 On a thick block of Poisson's ratio  $\nu_p$ , *Sánchez-Sesma et al.* [2011] give  $\left(\frac{\mathcal{H}}{\mathcal{V}}\right)_{\text{diffuse}} \approx 1.245 +$   
 529  $0.348\nu_p$ . Due to statistical assumptions, the diffuse method leads to larger uncertainties  
 530 on the results compared to that based on the energy flux [*Farin et al.*, 2015]. However,

531 it is the only method that can be applied when the first arrival can not be distinguished  
532 from its side reflections, as for example in the marble block (Figure 6f).

## 4.2. Comparison with Synthetic Signals

533 We compare the measured vibration acceleration  $a_z(r, t)$  with a synthetic signal which  
534 is the time convolution of *Hertz* [1882]'s force of elastic impact (Figure 1b with  $\alpha = 0$ )  
535 with the Green's function [equations (3) and (4)] (Figures 5e to 5h and 6e to 6h).

536 A good agreement is observed in terms of amplitude and frequencies on the PMMA  
537 plate but the agreement is less satisfactory on the other substrates. On glass, only the  
538 beginning of the signal is well reproduced by the theory (Figure 5f). A resonance of  
539 the accelerometer coupled to the glass plate for 38 kHz could explain why the recorded  
540 vibration lasts longer than the synthetic one (Figure 5f). This effect clearly appears on the  
541 Fourier transform of the signal with a peak of energy around 38 kHz (Figure 5h). Using a  
542 laser Doppler vibrometer that measures the exact surface vibration speed but with a much  
543 lower sensitivity than the accelerometers, we determined that the resonance overestimates  
544 the vibration energy by a factor of 4. To compensate this effect, we divide the measured  
545 radiated elastic energy  $W_{el}$  by this factor. On concrete, the synthetic is significantly  
546 different than the recorded signal in terms of higher amplitude and frequencies (Figures  
547 6f and 6h). The impact may be not completely normal to the surface owing to the surface  
548 roughness, and this could reduce the energy on the normal component, as discussed later  
549 in section 5. On marble, the frequencies of the measured signal are close to that of the  
550 synthetic one but the amplitude is higher than in theory, probably because side reflections  
551 arrive before the end of the first arrival (Figures 6e and 6g). This has no consequence on  
552 the estimation of the radiated elastic energy  $W_{el}$  for this block because we use the diffuse

553 method [equation (43)]. Note that the peaks of energy for  $f > 50$  kHz in the synthetic  
554 spectrum on the concrete and marble block are not visible in the recordings, because the  
555 accelerometers are not sensitive in this frequency range (see Appendix B).

### 4.3. Experimental Test of the Analytical Scaling Laws

#### 556 4.3.1. Radiated Elastic Energy

557 Regardless of the bead material, the measured radiated elastic energy  $W_{el}$  on the PMMA  
558 and glass plates matches well with the theoretical energy  $W_{el}^{th}$  predicted in equation (23)  
559 for an elastic impact, with  $C_{plate} = 1.21$  (Figure 7). For the smallest and the largest  
560 beads investigated, however, the data points separate from the theoretical line and the  
561 discrepancy can reach a factor of 5. This is clearer for steel beads (Figures 7c and 7g)  
562 and for glass beads on the glass plate (Figure 7e).

563 On blocks, the theory predicts that  $W_{el}^{th} \propto mV_z^{13/5}$  (equation (24) and Table 1). The  
564 experimental data of beads impacts on the concrete and marble blocks follow qualitatively  
565 this law (Figure 8). In most of the experiments, however, the measured energy  $W_{el}$  is lower  
566 than in theory. Moreover, on concrete, the measured radiated elastic energy  $W_{el}$  separates  
567 from the theoretical trend for the smallest and the largest beads investigated (Figures 8a,  
568 8b and 8c). The discrepancy with the theory on Figures 7 and 8 is interpreted in the  
569 discussion.

570 Surprisingly, the elastic energy  $W_{el}$  radiated by the impacts of granite gravels follows  
571 well the scaling law in  $m^{5/3}V_z^{11/5}$  on plates (Figures 7d and 7h) and in  $mV_z^{13/5}$  on blocks  
572 (Figures 8d and 8h). The measured energy  $W_{el}$  is however smaller than in theory, by a  
573 factor of 2 on plates and up to 10 times smaller on blocks. The experiments with gravels  
574 show that Hertz's analytical model of elastic impact, established for spheres, can also

575 describe at first order the impact dynamics of impactors with a complex shape. As a  
 576 consequence, we expect that it may also be applied for natural rockfalls.

#### 577 4.3.2. Characteristics Frequencies

578 We compute the mean frequency  $f_{mean}$  and the bandwidth  $\Delta f$  using equations (25) and  
 579 (26), respectively (Figure 9). Note that the seismic signals generated by bead impacts in  
 580 our experiments contain much higher frequencies (1 Hz - 100 kHz) than those recorded  
 581 for natural rockfalls (1 Hz - 50 Hz) [e.g. *Deparis et al.*, 2008; *Hibert et al.*, 2011]. This is  
 582 because the bead diameters are in average smaller than the diameter of natural boulders,  
 583 that could be from a few millimeters to a few meters large. In addition, the sampling  
 584 frequency is much higher and high frequencies are much less attenuated in our experiments  
 585 than on the field.

586 On the glass plate, as the accelerometers are not sensitive to frequencies larger than  
 587 50 kHz, the frequencies computed with these sensors saturate to about 40 kHz for the  
 588 smallest beads i.e., the smallest impact durations  $T_c$  (black crosses on Figures 9c and  
 589 9d). Therefore, the accelerometers type 8309 are used only for the impacts that generate  
 590 energy below 50 kHz. For the signals of higher frequencies, we use in parallel piezoelectric  
 591 ceramics (MICRO-80, *Physical Acoustics Corporation*) sensitive between 100 kHz to 1  
 592 MHz. These last sensors can however not be used to quantify the radiated elastic energy  
 593  $W_{el}$  since they are not very sensitive to frequencies lower than 100 kHz.

594 Regardless of the bead material, the frequencies of the signals generated by impacts  
 595 on PMMA, glass and marble collapse well within  $\pm 20\%$  with the theoretical scaling laws  
 596 of Table 2 as a function of the duration of impact  $T_c$  (Figures 9a to 9d, 9g and 9h).  
 597 The agreement is better for the frequency bandwidth  $\Delta f$  than for the mean frequency



598  $f_{mean}$ . The agreement is also very satisfactory for the granite gravels of complex shape,  
 599 even though the theoretical values of the frequencies were computed using Hertz's impact  
 600 model for a sphere (see section 2.2.2).

601 In concrete, the wavelength  $c_R/f \approx 1$  cm for frequencies around 40 kHz, which is of the  
 602 order of the size of the heterogeneities. High frequencies  $f > 40$  kHz are therefore strongly  
 603 attenuated during wave propagation in this block. This could explain the discrepancy with  
 604 the theory for these frequencies on Figure 9e.

### 605 4.3.3. Estimating Impact Properties from the Seismic Signal

606 We use equations (27) to (30) with the coefficients for an elastic impact  $C_{plate} = 1.21$   
 607 and  $C_{block} = 0.02$  to retrieve the mass  $m$  and the impact speed  $V_z$  of the impactors in  
 608 our experiments. The agreement with the real values is correct, within a factor of 2 for  
 609 the mass  $m$  (Figure 10a) and within a factor of 3 for the impact speed  $V_z$  (Figure 10b),  
 610 both on smooth thin plates and rough thick blocks. For impacts of rough gravels on the  
 611 two plates, the predicted values are still close to the real ones, with a factor of 1.5, even  
 612 when inelastic dissipation occurs. The underestimation of  $m$  and  $V_z$  in certain cases is  
 613 consistent with the aforementioned discrepancy of the radiated energy  $W_{el}$  with theory  
 614 (Figures 7 and 8).

615 It is therefore possible to have an estimation of the mass  $m$  and the impact speed  
 616  $V_z$  of an impactor on a plate and on a block from the characteristics of the generated  
 617 seismic signal, with less than an order of magnitude from the real values, using only *Hertz*  
 618 [1882]'s analytical model of elastic impact. This method only requires to know the elastic  
 619 parameters of the involved materials.

#### 4.4. Energy Budget of the Impacts

620 Inelastic losses during an impact can reduce the energy radiated in the form of elastic  
 621 waves  $W_{el}$  compared to that predicted by *Hertz* [1882]’s model (see section 2.2.1). This  
 622 may explain part of the discrepancy observed between the measured radiated elastic energy  
 623  $W_{el}$  and its theoretical value  $W_{el}^{th}$  on Figures 7 and 8, and consequently between the values  
 624 of the masses  $m$  and speeds  $V_z$  inverted from seismic signals and their real values on Figure  
 625 10. In order to interpret these discrepancies, we establish in this section an energy budget  
 626 of the impacts.

627 For that purpose, we compare on Figures 11 and 13 the measured radiated elastic energy  
 628  $W_{el}$  (empty symbols) with the total energy lost during the impact  $\Delta E_c$ , estimated with  
 629 the coefficient of restitution  $e$  (full symbols). The difference  $\Delta E_c - W_{el}$  is likely lost in  
 630 inelastic processes, such as viscoelastic dissipation or plastic deformation. This allows us  
 631 to establish an energy budget of the impacts (Figures 12 and 14).

632 Furthermore, we also compare the measured radiated energy  $W_{el}$  with the theoretical  
 633 one – noted  $W_{el}^{th}$ , red line on Figures 11 and 13 –, predicted by the scaling law in Table  
 634 1 for an elastic impact, with  $C_{plate} = 1.21$  and  $C_{block} = 0.02$ , respectively. Note that  
 635 on plates, we take into account the dependence of  $C_{plate}$  coefficient to  $\lambda_Z$  parameter for  
 636 large beads (see section 2.1.1.2 and Figure 2a). The corrected theoretical elastic energy  
 637 on plates is noted  $W_{el}^{th'}$  on Figure 11. The discrepancy with theory is discussed in section  
 638 5.1.

##### 639 4.4.1. Energy Budget on Smooth Thin Plates

640 On smooth thin plates, the energy  $\Delta E_c$  lost by the bead during an impact is mostly  
 641 radiated in elastic waves ( $W_{el}$ ) or dissipated by viscoelasticity during the impact ( $W_{visc}$ )  
 642 (Figures 11 and 12).

643 More energy is radiated in elastic waves as the bead mass  $m$  and the ratio of the bead  
 644 diameter  $d$  on the plate thickness  $h$  increase, regardless of the elastic parameters (empty  
 645 symbols on Figures 11 and 12). For the smallest beads investigated, only 0.1% to 0.3%  
 646 of the impact energy  $E_c$  is radiated in elastic waves. In contrast, the impact energy  $E_c$   
 647 can be almost entirely converted into elastic waves when the bead diameter  $d$  is greater  
 648 than the plate thickness  $h$  (Figure 11c). For large beads, the measured ratio of  $W_{el}/E_c$   
 649 is close to the theoretical ratio  $W_{el}^{th'}/E_c$  (full red line on Figure 11), but diverges as the  
 650 bead diameter  $d$  decreases.

651 We adjust the viscoelastic parameter  $D$  in equation (35) to match the theoretical ex-  
 652 pression of the lost energy ratio  $\Delta E_c/E_c = W_{el}^{th'}/E_c + W_{visc}/E_c$  (thick green line on Figure  
 653 11) with the variation of  $1 - e^2$  (full symbols). The agreement is found to be the best for  
 654 values of  $D$  ranging from 35 ns to 580 ns (Table 5).

655 The adjustment of  $D$  with experimental data allows us to quantify the viscoelastic  
 656 energy  $W_{visc}$  (blue line on Figure 11). More energy is lost by viscoelastic dissipation  
 657 as the bead mass  $m$  and the ratio  $d/h$  decrease and this is almost the sole process of  
 658 energy loss when the bead diameter  $d$  is smaller than  $0.2h$  (Figure 12). The transition  
 659 from a viscoelastic impact towards an elastic impact is observed for the critical mass  
 660  $m_c \approx 8D\sqrt{B\rho_p h}$ , as predicted in section 2.3.2 (at the crossing between the red and blue  
 661 lines on Figure 11). Interestingly, a bouncing bead loses less of its initial energy  $E_c$  for  
 662 masses  $m$  close to the critical mass  $m_c$ .

663 For the largest beads of glass and steel, some energy is likely lost in plastic deformation  
 664 of the softer material involved (Figure 12). As a matter of fact, we observed small inden-  
 665 tations on the surface of the plates after the impacts of these beads but not for polyamide  
 666 beads.

667 Note that the energy budget is very different for impacts of rough gravels on the same  
 668 plates. Indeed, the ratio  $W_{el}/E_c$  is  $3.3\% \pm 1.8\%$  regardless of the gravel mass  $m$ . Moreover,  
 669 about  $33\% \pm 17\%$  of the initial energy is lost in translational energy of rebound and  
 670  $13\% \pm 11\%$  is converted into rotational energy of the gravel. As a matter of fact, half of  
 671 the gravel's initial energy is in average lost in plastic deformation. (see Appendix C for  
 672 more details).

#### 673 4.4.2. Energy Budget on Rough Thick Blocks

674 On the rough thick blocks, the energy budget is very different than on the smooth  
 675 plates (Figures 13 and 14). Indeed, a much smaller proportion of energy seem to be  
 676 lost in elastic waves and in viscoelastic dissipation. The rest is likely dissipated by other  
 677 processes such as plastic deformation, adhesion or rotational modes of the bead owing to  
 678 surface roughness.

679 The measured radiated elastic energy  $W_{el}$  represents only from 0.01% to 2% of the  
 680 impact energy  $E_c$ , regardless of the bead mass  $m$  (empty symbols on Figure 13). Theory  
 681 predicts that the ratio  $W_{el}^{th}/E_c$  is independent of the mass  $m$  (red line). However, the  
 682 measured ratio  $W_{el}/E_c$  slightly increases with bead mass  $m$  on concrete and decreases on  
 683 marble for different reasons explained in the discussion.

684 Contrary to plates, it is difficult here to determine what proportion of the lost en-  
 685 ergy  $\Delta E_c$  is dissipated by viscoelasticity and what proportion is lost in other processes.

686 However, one remarks that  $1 - e^2$  increases when the mass  $m$  decreases (full symbols  
 687 on Figure 13). This variation may be due to viscoelastic dissipation which is stronger  
 688 when the bead mass  $m$  decreases [equation (35)]. We make the strong assumption that  
 689 the percentage of energy lost in other processes  $W_{other}/E_c$  is constant and independent  
 690 of the bead mass  $m$ . We then adjust the viscoelastic coefficient  $D$  (Table 5) to fit  
 691  $\Delta E_c/E_c = W_{el}^{th}/E_c + W_{visc}/E_c + W_{other}/E_c$  (thick green line on Figure 13) with the vari-  
 692 ation of  $1 - e^2$  (full symbols). This allows to quantify the energy  $W_{visc}$  lost in viscoelastic  
 693 dissipation (blue line).

694 In the case where no other energy losses than elastic waves radiation or viscoelastic  
 695 dissipation occur, we predicted that the ratios  $W_{el}/\Delta E_c$  and  $W_{visc}/\Delta E_c$  should increase  
 696 and tend towards 100% when the mass  $m$  increases and decreases, respectively [equations  
 697 (38) and (39)]. Here, elastic waves radiation and viscoelastic dissipation follow the same  
 698 dependence on the mass than that predicted but represent respectively from 0.03% to  
 699 5% and from 2% to 40 % of the lost energy  $\Delta E_c$  only (Figure 14). For impacts on rough  
 700 substrates as the two blocks investigated here, but also on the field, it is therefore important  
 701 to take into account the energy  $W_{other}$  lost in other processes. In our experiments, this  
 702 energy seems to be an increasing percentage of the lost energy  $\Delta E_c$ , from 50% to more  
 703 than 99%, as the bead mass  $m$  increases (Figure 14).

#### 704 4.4.3. Evaluation of the Energy Budget for Natural Rockfalls

705 The energy budget of impacts on rough blocks in our laboratory experiments can be  
 706 used to extrapolate that of natural rockfalls. On the field, the impactors masses varies  
 707 from a few grams to a few tons and drop heights varies from a few centimeters to several  
 708 tens of meters. Owing to strong energy dissipation in such complex media, only impacts of

709 large masses can be detected by seismic methods. Viscoelastic dissipation should therefore  
 710 be negligible in most situations encountered on the field. For example, we can estimate  
 711 the energy lost in viscoelastic dissipation for a granite gravel of  $m = 100$  g impacting the  
 712 ground with impact speed  $V_z = 10$  m s<sup>-1</sup> using equation (35) with the coefficient  $D = 80$  ns  
 713 of glass, which has similar properties than granite, and a typical Young's modulus  $E_p = 10$   
 714 MPa for the ground [*Geotechdata.info*, 2013]. It results that the viscoelastic energy  $W_{visc}$   
 715 represents only 0.04% of the impact energy  $E_c$ , which is negligible. Moreover, it should  
 716 be even smaller for larger masses  $m$ . The energy  $W_{plast}$  dissipated in plastic deformation  
 717 of the ground or of the impactor is expected to be much more significant on the field  
 718 than in our laboratory experiments and even more so when the mass  $m$  increases because  
 719 large stresses are applied on damaged materials with a low yield stress. For such impacts  
 720 with a rough contact, the energy  $W_{plast}$ , in addition to other energy lost in rotation and  
 721 translational modes of the impactor, should then represent almost all of the lost energy  
 722  $\Delta E_c$  (see Appendix C). Consequently, the ratio of the radiated elastic energy over the lost  
 723 energy  $W_{el}/\Delta E_c$  may not exceed a few percents. For example, for impacts of beads on  
 724 the rough concrete block, for which plastic deformation is significant, the ratio  $W_{el}/\Delta E_c$   
 725 seems to saturate to  $2\% \pm 1\%$  for  $m \simeq 1$  g and then decreases (Figure 14a).

## 5. Discussion

### 5.1. Discrepancy from Hertz's Model

726 The characteristic frequencies of the signal generated by an impact do not significantly  
 727 deviate from *Hertz* [1882]'s prediction when the impact is inelastic (Figure 9). On the  
 728 contrary, in some experiments, the measured radiated elastic energy  $W_{el}$  diverges from  
 729 that (noted  $W_{el}^{th}$ ) given by the scaling laws in Table 1 (Figures 7 and 8). As a consequence,

730 the masses  $m$  and speeds  $V_z$  retrieved from the measured signal in our experiments using  
 731 the elastic model deviate from their real values (Figure 10). Let us discuss here the  
 732 observed discrepancy.

### 733 5.1.1. Small Bead Diameters

734 On smooth thin plates, for small bead diameters, viscoelastic dissipation is the major  
 735 energy loss process (Figure 12). For a steel bead of diameter 1 mm impacting the glass  
 736 plate, using equation (19) with  $D = 35$  ns (see Table 5), the coefficient  $C_{plate}$  is found to be  
 737 equal to 1.15 instead of 1.21 for an elastic impact (see Figure 2a). Thus, the viscoelastic  
 738 impact theory predicts that the radiated elastic energy  $W_{el}^{th}$  should be only of 5% smaller  
 739 than for an elastic impact, which is negligible compared with the observed difference of  
 740 73% (Figure 7g).

741 The major source of discrepancy is probably due to the fact that our sensors are band  
 742 limited up to 50 kHz. Indeed, for the 1-mm bead, 50% of the radiated energy is in theory  
 743 higher than 50 kHz (see Appendix B). The remaining 23% may be lost in adhesion of the  
 744 bead on the plate during the impact. In addition, some energy may be lost in electro-  
 745 staticity or capillarity, which are greater for the smallest beads [Andreotti *et al.*, 2013].  
 746 The discrepancy is totally explained by the limited bandwidth of the accelerometers for  
 747 a steel bead of diameter  $d = 2$  mm on the glass plate: about 30% of the energy is over  
 748 50 kHz and the measured energy  $W_{el}$  is 35% smaller than  $W_{el}^{th}$  (Figure 7g). Similarly, on  
 749 concrete, for a steel bead of diameter  $d = 2$  mm, the theory predicts that only 17% of  
 750 the radiated elastic energy is below 50 kHz. As a consequence, the measured energy  $W_{el}$   
 751 represents only 17% of the theoretical energy  $W_{el}^{th}$  (Figure 8c). For greater bead diameters,  
 752 both measured and theoretical energies are contained below 50 kHz and the agreement

753 with elastic theory is better (Figures 7 and 8). In contrast, on marble the radiated elastic  
754 energy is closer to the theory for the smallest beads (Figures 13d to 13f). For small bead  
755 diameters, less wave reflections occur within the block and the measured energy may  
756 therefore be overestimated because the diffuse field is not completely set [*Farin et al.*,  
757 2015].

758 This emphasize the importance for future applications to use seismic sensors sensitive  
759 in the widest frequency range as possible. In cases where we can not measure the highest  
760 frequencies of the seismic vibration generated by an impact, note that it is possible to  
761 retrieve the momentum  $mV_z$  of the impactor from the low frequency content of measured  
762 amplitude spectrum (see Appendix D).

### 763 5.1.2. Large Bead Diameters

764 On smooth thin plates, the divergence of the measured radiated elastic energy  $W_{el}$  from  
765 the theoretical one  $W_{el}^{th}$  for large bead diameters is partly compensated when we take into  
766 account the decrease of the coefficient  $C_{plate}$  when the parameter  $\lambda_Z$  increases (Figures  
767 2a and 11). However, in some experiments,  $W_{el}$  is still smaller than the theory when the  
768 bead diameter  $d$  is larger than the plate thickness  $h$  (Figures 11c, 11d and 11f). This  
769 difference may be due to plastic deformation which is more likely to occur for the largest  
770 beads investigated.

### 771 5.1.3. Impacts with a Rough Contact

772 Two complementary effects can explain the discrepancy of the measured radiated elastic  
773 energy with theory for impacts of spherical beads on the two rough blocks and for impacts  
774 of gravels (Figures 7d, 7h and 8).



775 First, plastic deformation is a likely cause for measuring a smaller radiated elastic energy  
776 than in theory on the blocks. If  $P_Y/P_0 = 0.6$  in the elasto-plastic model, the radiated  
777 elastic energy predicted in Table 1 is two times smaller than for an elastic impact because  
778 the coefficient  $C_{block} \approx 0.01$  instead of 0.02 (Figure 2b). This factor of 2 corresponds to  
779 that observed between the measured energy  $W_{el}$  and the theoretical one  $W_{el}^{th}$  for impacts of  
780 glass and steel beads on the concrete block (Figures 8a and 8c). Measuring the discrepancy  
781 of the radiated elastic energy from elastic theory could then be a mean to estimate the  
782 dynamic yield strength  $P_Y$  of a material. For example, for a steel bead of diameter  $d = 5$   
783 mm dropped from height  $H = 10$  cm on concrete, the maximum stress is  $P_0 \approx 300$  MPa  
784 and, if  $P_Y/P_0 = 0.6$ , the dynamic yield strength would be  $P_Y \approx 180$  MPa, which is greater  
785 than the typical values of  $P_Y$  for concrete [20-40 MPa, *The Engineering Toolbox*, 2014]  
786 but of the same order of magnitude.

787 An additional process can accommodate the discrepancy. If a spherical bead impacts a  
788 rough surface or as a gravel impacts a flat surface, the equivalent radius of contact may  
789 be smaller than the radius of the impactor (Figure 15). Table 1 shows that the radiated  
790 elastic energy  $W_{el}$  increases with the impactor radius  $R$  as  $R^5$  on plates and as  $R^3$  on  
791 blocks. Then, if the radius of contact  $R$  is only 1.15 smaller on plates, the theoretical  
792 radiated elastic energy  $W_{el}$  is two times smaller, and this explain the discrepancy observed  
793 for gravels on the plates (Figures 7d and 7h). On blocks, if the effective radius of contact  $R$   
794 is 2.1 times smaller, the radiated elastic energy  $W_{el}$  is 10 times smaller, that could explain  
795 the small energy values measured on the marble block (Figures 8e to 8h). The radius of  
796 contact  $R$  should be even smaller when gravels impacts the rough blocks and the radiated  
797 elastic energy  $W_{el}$  is then smaller (Figures 8d and 8h). By comparison, the characteristic

798 frequencies  $f_{mean}$  and  $\Delta f$  are inversely proportional to the radius  $R$  (because  $T_c \propto R$ )  
 799 and are therefore less affected by a change in this radius than the radiated elastic energy  
 800  $W_{el}$ . This is visible on Figure 9 because the frequencies of the signal emitted by gravels  
 801 are close to that of spherical beads.

802 As the effective radius of contact decreases for a given mass  $m$ , the stresses are con-  
 803 centrated on a smaller area during the impact and plastic deformation is more likely to  
 804 occur (see Appendix C). Interestingly, even though the energy lost in plastic deformation  
 805 is very important for impacts of gravels and on the rough blocks, the measured radiated  
 806 elastic energy  $W_{el}$  and frequencies  $f_{mean}$  and  $\Delta f$  still follow well the scaling laws in mass  
 807  $m$  and impact speed  $V_z$  predicted using Hertz's model of impact of a sphere on a plane  
 808 (Figures 7, 8 and 9). Therefore, we expect that Hertz's model should be still valid at  
 809 first order on the field and, consequently, that the radiated elastic energy  $W_{el}$  should be  
 810 proportional to  $mV_z^{13/5}$  and that the characteristic frequencies  $f_{mean}$  and  $\Delta f$  should be  
 811 proportional to  $1/T_c \propto m^{-1/3}V_z^{1/5}$ . The problem is however to determine the coefficients  
 812 of proportionality in these relations because they depend on the rheological parameters  
 813 of the impactor and the ground (Table 1), on the fact that is impact is elastic or inelastic  
 814 (Figures 2 and 3) and on the roughness of contact, which are each extremely difficult to  
 815 estimate practically. A solution may be to calibrate the coefficients of proportionality of  
 816 these relations on a given site by dropping some boulders of known mass  $m$  and estimat-  
 817 ing their impact speed  $V_z$ . Once calibrated, these laws can be inverted as in section 2.2.3  
 818 and used to retrieve the masses  $m$  and impact speeds  $V_z$  of other rockfalls on the same  
 819 site from the generated seismic signals. The advantage of this method is that it is not  
 820 necessary to know the elastic parameters of the ground. Even so, energy attenuation as a

821 function of frequency during wave propagation within the substrate need to be evaluated  
822 in order to correct the measured signals.

## 5.2. Errors on the Estimation of the Masses and Impact Speeds

823 Here we comment the errors on our estimation of the impactors masses from measured  
824 seismic signals in Figure 10. These errors are greater than that of *Buttle et al.* [1991]  
825 who managed to size sub-millimetric particles in a stream with a standard deviation less  
826 than 10%. However, their estimations were based on the impact force and duration on  
827 the direct compressive wave, measured at the opposite of the impact on the target block.  
828 Practically, this method is difficult to apply on the field because seismic stations are at  
829 the surface. Furthermore, the force and duration of the impact are more complicated  
830 to estimate from the seismic signal than the radiated elastic energy and the frequencies  
831 because it requires a deconvolution process that induce additional errors [e.g., *McLaskey*  
832 *and Glaser*, 2010]. Our method has the advantage to be not intrusive and in principle  
833 exportable to field problems.

## 5.3. Application to Natural Rockfalls

834 *Dewez et al.* [2010] conducted field scale drop experiments of individual basalt boulders  
835 on a rock slope in Tahiti, French Polynesia. The main objective of this study was to  
836 estimate hazards associated with rockfalls in a volcanic context. Boulders trajectory was  
837 optically monitored using two cameras with 50 frames per seconds. A photogrammetry  
838 technique then allowed the authors to compute the position of each boulder in time with  
839 an error smaller than the boulder radius [*Dewez et al.*, 2010]. In parallel, the seismic signal  
840 generated by boulders impacts on the ground was recorded with a sampling frequency of

841 100 Hz by a board band seismometer type *STS* located a few tens of meters away. Here  
842 we want to observe how the elastic energy radiated by boulder impacts scales with the  
843 boulder's mass and speed in this natural context.

### 844 5.3.1. Comparison of Field Measurements with Hertz's Prediction

845 The waves generated by the impacts propagate in a very damaged and complex medium  
846 that may involve several layers of different density. In this medium, viscous attenuation  
847 of energy can be very strong, especially for high frequencies. For example, waves of  
848 frequency 100 Hz only propagate in the first centimeters or meters deep below the surface.  
849 Knowing the attenuation as a function of frequency, and assuming some sensitivity /  
850 noise level for the sensor, it is possible to correct for this attenuation for all frequencies  
851 where the amplitude is above the noise level. The corrected amplitude spectrum should  
852 then be equivalent to the emitted spectrum, assuming that all the frequencies have been  
853 recorded. The attenuation of energy as a function of frequency can be evaluated, for  
854 example, by measuring the signal emitted by a given impact at different distances, as we  
855 did in our laboratory experiments [*Farin et al.*, 2015]. Unfortunately, no estimation of  
856 the attenuation has been conducted in this field study. We therefore assume a classical  
857 attenuation model of energy with distance  $r$  and multiply the measured signals by the  
858 factor  $\exp(\gamma(f)r)$ , with  $\gamma(f) = \pi f / Qc_R$  [*Aki and Richards*, 1980]. We use the quality  
859 factor  $Q = 10$ , which is of the order of the values obtained by *Ferrazzini and Aki* [1992]  
860 in the similar context of Kilauea volcano in Hawaiï.

861 We first focus on the seismic signals emitted by the impacts of a boulder of mass  $m = 326$   
862 kg at  $r \simeq 30$  m from the seismometer (Figure 16a). The signals have a short duration  
863  $\sim 0.8$  s and are impulsive, as the ones generated by bead impacts (e.g., Figure 6c). The

864 impacts excite a frequency range from  $\sim 10$  Hz to 40 Hz (Figure 16b). Most of the  
 865 recorded seismic spectra lies between 10 Hz and 20 Hz with a peak frequency  $f_{peak} \approx 15.5$   
 866 Hz, a mean frequency  $f_{mean} \approx 18.4$  Hz and a bandwidth  $\Delta f \approx 18.3$  Hz (Figures 16b and  
 867 16c).

868 We compare the measured spectrum with a synthetic amplitude spectrum predicted  
 869 by *Hertz* [1882]’s theory of impact using equation (2). The Green’s function used in the  
 870 computation depends on the excited mode. *Deparis et al.* [2008], *Dammeier et al.* [2011]  
 871 and *Lévy et al.* [2015] showed that rockfall events generate principally Rayleigh surface  
 872 waves. Rayleigh waves develop in far field, i.e. for  $kr \gg 1$ , where  $k = 2\pi f/c_R$  is the  
 873 wave number [*Miller and Pursey*, 1954; *Gimbert et al.*, 2014; *Farin et al.*, 2015]. In the  
 874 Piton de la Fournaise volcano, Reunion Island, where the ground has a similar structure  
 875 as in Tahiti, the phase speed  $c_R$  is  $800 \text{ m s}^{-1}$  [*Hibert et al.*, 2011]. We use here the same  
 876 phase speed  $c_R$  and estimate that  $kr \gg 1$  when the frequency  $f$  is greater than about 4  
 877 Hz. Since the recorded seismic energy is mostly between 10 Hz to 40 Hz, we can therefore  
 878 reasonably use the far field Green’s function of Rayleigh waves of equation (4) convolved  
 879 with *Hertz* [1882]’s impact force to compute the synthetic spectrum (Figure 16c).

880 The characteristics of the impactor are  $R = 0.35$  m,  $m = 326$  kg and  $V_z = 11$  m  
 881  $\text{s}^{-1}$ . We assume a typical Young’s modulus  $E_p = 10$  MPa for a loose soil such that  
 882 observed on the slope [*Geotechdata.info*, 2013]. *Hertz* [1882]’s elastic theory then predicts  
 883 that the duration of impact should be  $T_c \simeq 0.035$  s [equation (9)]. For Rayleigh surface  
 884 waves, the mean frequency should therefore be  $f_{mean} = 1/T_c \simeq 28$  Hz and the bandwidth  
 885  $\Delta f = 0.6/T_c \simeq 17$  Hz, which are close to the measured values (Table 2 and Figure 16c).

886 The amplitude of the synthetic spectrum is similar to that of the measured spectrum  
 887 except around 15 Hz where a peak of energy is observed in the measured spectrum (Figure  
 888 16c). The peak of energy may be due to a resonance around 15 Hz of the seismometer or  
 889 of the first sediment layers because it is observed on every measured spectra [*Schmandt*  
 890 *et al.*, 2013; *Farin*, 2015]. The shape of the measured and synthetic spectrum is very  
 891 different. This may be due to plastic deformation, which is very important for impacts  
 892 on loose and fractured soil.

### 893 5.3.2. Elastic Energy Radiated by Boulders Impacts

894 Despite the discrepancy between the theory and the measurement, we observe how the  
 895 elastic energy  $W_{el}$  radiated by the impacts of all boulders depends on the boulder mass  
 896  $m$  and impact speed  $V_z$ . The calculation of  $W_{el}$  is based on the integration of the energy  
 897 flux over a cylinder surrounding the impacts [*Hibert et al.*, 2011; *Farin et al.*, 2015]:

$$898 \quad W_{el} = 4\pi r h \rho c_R \int_0^{+\infty} |\tilde{V}(r, f)|^2 \exp(\gamma(f)r) df, \quad (44)$$

899 where  $h = c_R/f$  is the Rayleigh wavelength and  $|\tilde{V}(r, f)|^2 = |\tilde{V}_X(r, f)|^2 + |\tilde{V}_Y(r, f)|^2 +$   
 900  $|\tilde{V}_Z(r, f)|^2$  is the sum of the squared time Fourier transforms of the vibration speeds in  
 901 the three directions of space  $v_X(r, t)$ ,  $v_Y(r, t)$  and  $v_Z(r, t)$ , respectively. The coefficient  
 902  $\gamma(f) = \pi f/Qc_R$  is the same than that used to compute the synthetic spectrum in the  
 903 previous section, with  $c_R = 800 \text{ m s}^{-1}$  and  $Q = 10$ .

904 The nature of the contact between the boulder and the ground during the impact plays  
 905 a crucial role on the transfer of the seismic energy. Therefore, we separated the “hard”  
 906 impacts, occurring on outcropping rock, from the “soft” impacts, occurring on loose soil  
 907 or on grass (Figures 16d to 16g). The measured radiated elastic energy  $W_{el}$  seems to be  
 908 proportional to the mass  $m$  as predicted analytically for impacts on thick blocks (Table 1

909 and Figure 16d). This dependence is clearer for “soft” impacts. However, the measured  
910 radiated elastic energy  $W_{el}$  does not scale well with the parameter  $mV_z^{13/5}$  derived from  
911 Hertz’s theory (Figure 16e). We adjust the power  $a$  of parameter  $mV_z^a$  to obtain a better fit  
912 with  $W_{el}$ . The best fit is observed for power  $a \simeq 0.5$ , i.e. with a much weaker dependence  
913 on the impact speed  $V_z$  than in theory, with  $W_{el} \propto V_z^{0.5}$  rather than  $W_{el} \propto V_z^{13/5}$  (Figure  
914 16f). The scaling law in  $V_z^{0.5}$  may be biased because boulders systematically impacted  
915 loose soil when they reached high speeds  $V_z$  while they often impacted outcropping rocks  
916 for lower speeds  $V_z$ . The energy transfer is lower for “loose” impacts than for “hard”  
917 impacts and this may then leads to the observed weaker dependence in  $V_z$  (Figure 16g).  
918 As a matter of fact, the mean ratio of the radiated elastic energy  $W_{el}$  over the kinetic  
919 energy  $\Delta E_c$  lost during the impacts is one order of magnitude higher for “hard” impacts  
920 than for “soft” impacts (Figure 16g). Interestingly, the ratio  $W_{el}/\Delta E_c$  is between  $10^{-4}$   
921 and  $10^{-1}$ , which is in agreement with the values observed by *Hibert et al.* [2011].

922 No clear dependence on  $m$  and  $V_z$  was observed for the characteristic frequencies of  
923 the signal  $f_{mean}$  and  $\Delta f$ . These frequencies are between 10 Hz and 30 Hz, regardless of  
924 the contact quality i.e., of the fact that the impact is “hard” or “soft” [see Figure 92 in  
925 Chapter 4 of *Farin, 2015*].

926 An explanation for the discrepancy between observed and theoretical elastic energy  $W_{el}$   
927 and for the fact that we did not observe any trend for the frequencies may be that we  
928 can not record frequencies higher than 50 Hz because the sampling frequency is 100 Hz.  
929 Impacts of boulders are expected to generate waves of higher frequencies. For exam-  
930 ple, *Helmstetter and Garambois* [2010] dropped a boulder of similar dimensions on the  
931 Séchilienne rockslide site in the French Alps. Seismic signals generated by the impacts

932 were sampled at 250 Hz by several seismic stations located a few tens of meters away.  
933 In the spectrogram of these signals, energy is visible up to 100 Hz. As we previously  
934 observed in laboratory experiments, when we do not measure the highest frequencies of  
935 the generated signal, the discrepancy between the theory and the measurement increases  
936 (e.g. for small masses  $m$  in Figures 8a to 8c). An other possibility is that the factor  
937  $\exp(\gamma(f)r)$ , with  $\gamma(f) = \pi f/Qc_R$ , may be too simple to describe the wave propagation in  
938 such a damaged medium. Indeed, multiple modes with different dispersion relations can  
939 be excited in different frequencies range in such layered media. However, the data are not  
940 sufficient to determine how wave disperse and attenuate within the ground on this specific  
941 site.

942 Owing to the large scattering of the seismic data, it is difficult to neither validate  
943 nor invalidate the applicability on the field of the analytical scaling laws developed in this  
944 paper. However, this study highlights several challenges that need to be addressed in order  
945 to be able to retrieve the impacts parameters in future seismic studies of boulder impacts.  
946 If the radiated elastic energy or the characteristics frequencies of the emitted signals are  
947 underestimated, this will lead to either overestimate or underestimate the masses and  
948 impact speed, as evidenced in our laboratory experiments (Figure 10). Therefore, one  
949 should measure as much as possible the entire energy spectrum emitted by the impacts  
950 and, to do so, use a high sampling frequency, ideally greater than  $3/T_c$  (see section 2.2.2).  
951 Moreover, because energy at high frequencies attenuate very rapidly in fractured media,  
952 one should record the signal as close as possible from the impacts. Finally, one should have  
953 a good knowledge of the elastic properties of the impactor and the ground in the vicinity  
954 of the impact, as well as within the ground i.e., its how it disperses and attenuates the



955 frequencies. This could be achieved using several seismic stations recording at different  
956 distances from the source.

## 6. Conclusions

957 We developed analytical scaling laws relating the characteristics of the acoustic signal  
958 generated by an impact on a thin plate and on a thick block (radiated elastic energy, fre-  
959 quencies) to the parameters of the impact: the impactor mass  $m$  and speed before impact  
960  $V_z$  and the elastic parameters. These laws were validated with laboratory experiments of  
961 impacts of spherical beads of different materials and gravels on thin plates with a smooth  
962 surface, which is an ideal case, and on rough thick blocks, which are closer to the case of  
963 the field. Viscoelastic and elasto-plastic dissipation occurred in the range of masses and  
964 impact speeds investigated. In these experiments, the radiated elastic energy is estimated  
965 from vibration measurements, independently of the other processes of energy dissipation.  
966 A number of conclusions can be drawn from our results:

967 1. The impactor mass  $m$  and speed  $V_z$  can be estimated from two independent pa-  
968 rameters measurable on the field of the seismic signal: the radiated elastic energy and a  
969 characteristic frequency, using equations (27) to (30). The estimations of  $m$  and  $V_z$  are  
970 close to the real values within a factor of 2 and 3, respectively, even when the impactor  
971 has a complex shape. If the radiated elastic energy is underestimated (respectively, over-  
972 estimated) by a factor of 10, the mass  $m$  and the impact speed  $V_z$  are underestimated  
973 (respectively, overestimated) by a factor of 1.5 and 2, respectively. We noted that the  
974 radiated elastic energy is smaller when the surface roughness increases because the ra-  
975 dius of contact is smaller. However, the signal characteristics measured during impacts of

976 rough impactors on rough surfaces follows well the scaling laws established for impacts of  
977 spherical beads on a plane surface.

978 2. We also established a quantitative energy budget of the impacts on the plates and  
979 blocks investigated and we estimated what should be this budget for natural rockfalls:

980 (i) On the smooth plates, elastic waves and viscoelastic dissipation are the main  
981 processes of energy losses. Viscoelastic dissipation is major for impactors of diameter  
982 less than 10% of the plate thickness while elastic waves radiation represents only from  
983 0.1% to 0.3% of the impact energy. When the bead diameter increases, the energy lost in  
984 viscoelastic dissipation decreases while the energy radiated in elastic waves increases. For  
985 beads of diameter larger than the plate thickness, almost all of the energy is radiated in  
986 elastic waves.

987 (ii) On the rough blocks, elastic dissipation represents only between 0.03% and 5%  
988 of the lost energy. In contrast, energy lost in other processes such as plastic deformation  
989 increases with the bead mass from 50% to more than 99% of the lost energy because of  
990 surface roughness. The energy dissipated in viscoelasticity decreases from 50% to 2% of  
991 the lost energy as the bead mass increases.

992 (iii) Most of the energy lost during a natural rockfall should be dissipated in plastic  
993 deformation or in translational or rotational modes of the impactors. Plastic or in general  
994 irreversible dissipation reduces the energy radiated in elastic waves and is difficult to  
995 quantify. That said, regardless of the impactor mass and speed, the energy radiated in  
996 elastic waves may not be more than a few percent of the impact energy. Energy lost in  
997 viscoelastic dissipation should be negligible in the range of masses detected by seismic  
998 stations on the field.

999 The impacts experiments with rough impactors on rough substrates demonstrated that  
1000 Hertz's model can be used to describe at first order the dynamics of an impact when the  
1001 contact surface is not plane. Thus, we expect that the simple analytical relations derived  
1002 in this paper between the characteristics of the impact and that of the emitted signal can  
1003 allow us to better understand the process of elastic waves generation by impacts on the  
1004 field. The major limitation for estimating the impact properties from the signal on the  
1005 field would certainly be the fact that a great part of the radiated energy is lost in high  
1006 frequencies during wave propagation in highly fractured media. Therefore, we encourage  
1007 future seismic studies of rockfalls to record signals as close as possible to the impacts and  
1008 to use a high frequency sampling. In addition, it is important to correct measured seismic  
1009 signals from wave dispersion and attenuation within the substrate. If these conditions are  
1010 fulfilled, the scaling laws derived in this study should provide estimates of the order of  
1011 magnitude of the masses and speeds of the impactors. Finally, in addition to direct field  
1012 applications, the scaling laws developed for plates can be also useful in the industry as a  
1013 non-intrusive technique to estimate the size and speed of particles in a granular transport  
1014 and in shielding problems.

**Appendix A: Demonstration of the Analytical Scaling Laws for the Radiated Elastic Energy**

1015 The objective of this Appendix is to demonstrate the analytical scaling laws showed in  
 1016 Table 1 for the radiated elastic energy  $W_{el}$  as a function of the impactor’s mass  $m$  and  
 1017 speed  $V_z$  for thin plates and thick blocks.

1018 The radiated elastic energy is defined by:

1019 
$$W_{el} = \int_{-\infty}^{+\infty} |F_z(t)|^2 Y_{el}(t) dt = 2 \int_0^{+\infty} |\tilde{F}_z(f)|^2 \tilde{Y}_{el}(f) df, \quad (A1)$$

1020 with  $\tilde{Y}_{el}(f)$  the radiation admittance, that has a different expression on thin plates and  
 1021 on thick blocks.

**A1. Thin Plates**

1022 On thin plates,  $\tilde{Y}_{el}(f)$  is independent of frequency  $f$  and is given by:

1023 
$$Y_{el} = \frac{1}{8\sqrt{B\rho_p h}}. \quad (A2)$$

1024 where  $B$  is the bending stiffness and  $\rho_p$  and  $h$  are the plate density and thickness, respec-  
 1025 tively.

1026 Therefore,

1027 
$$W_{el} = \frac{1}{8\sqrt{B\rho_p h}} \frac{F_0^2 \delta_{z0}}{V_z} \int_{-\infty}^{+\infty} |g(t^*)|^2 dt^*, \quad (A3)$$

1028 with  $t^* = \delta_{z0}t/V_z$  and where  $g(t^*)$  is the shape function represented on Figures 1b and 1c.  
 1029 The integral in this equation is noted  $C_{plate}$  and depends on the inelastic parameters  $\alpha$   
 1030 and  $P_Y/P_0$  i.e., of the fact that the impact is elastic, viscoelastic or elasto-plastic (Figures  
 1031 2a and 2b). For an elastic impact,  $C_{plate} = 1.21$ .

1032 Developing  $F_0$  and  $\delta_{z0}$  as functions of the impact parameters using their expressions in  
 1033 equations (5) and (8), respectively, we get:

$$1034 \quad \frac{F_0^2 \delta_{z0}}{V_z} = \left(\frac{4}{3}\right)^{1/3} \left(\frac{5}{4}\right)^{8/5} \pi^{-1/15} \rho_s^{-1/15} E^{*2/5} m^{5/3} V_z^{11/5}. \quad (\text{A4})$$

1035 Finally, equations (A3) and (A4) give the scaling law relating the radiated elastic energy  
 1036  $W_{el}$  to the impact parameters on thin plates:

$$1037 \quad W_{el} = a_1 C_{plate} m^{5/3} V_z^{11/5}, \quad (\text{A5})$$

1038 with  $a_1 \approx 0.18 E^{*2/5} / (\rho_s^{1/15} \sqrt{B \rho_p h})$ .

## A2. Thick Blocks

1039 On thick blocks, the radiation admittance  $\tilde{Y}_{el}(f)$  was computed in time Fourier domain  
 1040 by *Miller and Pursey* [1955]:

$$1041 \quad \tilde{Y}_{el}(f) = \frac{2\pi \xi^4 \beta f^2}{\rho_p c_P^3}, \quad (\text{A6})$$

1042 where  $\xi = \sqrt{2(1 - \nu_p)/(1 - 2\nu_p)}$ ,  $c_P$  is the compressive wave speed and  $\beta$  is the imaginary  
 1043 part of

$$1044 \quad \int_0^X \frac{x \sqrt{x^2 - 1}}{f_0(x)} dx, \quad (\text{A7})$$

1045 with  $f_0(x) = (2x^2 - \xi^2)^2 - 4x^2 \sqrt{(x^2 - 1)(x^2 - \xi^2)}$  and  $X$ , a real number greater than the  
 1046 positive real root of  $f_0$ . The coefficient  $\beta$  depends only on the Poisson's ratio  $\nu_p$  (Figure  
 1047 17, see the Appendix of *Farin et al.* [2015] for details on the computation of  $\beta$ ).

1048 Therefore,

$$1049 \quad W_{el} = \frac{4\pi \xi^4 \beta F_0^2 V_z}{\rho_p c_P^3 \delta_{z0}} \int_0^{+\infty} f^{*2} |\tilde{g}(f^*)|^2 df^*, \quad (\text{A8})$$

1050 with  $f^* = V_z f / \delta_{z0}$  and  $\tilde{g}(f^*)$  is the time Fourier transform of the function  $g(t^*)$  represented

1051 on Figures 1b and 1c. We note  $C_{block}$  the integral in this equation.  $C_{block}$  depends on the

1052 inelastic parameters  $\alpha$  and  $P_Y/P_0$  (Figures 2a and 2b). With an impact force  $F_z(t)$  given  
 1053 by *Hertz* [1882]’s elastic theory i.e., for  $\alpha = 0$  and  $P_Y/P_0 = 1$ , we have  $C_{block} = 0.02$ .

1054 If we develop  $F_0$  and  $\delta_{z0}$  as functions of the impact parameters, we get:

$$1055 \quad \frac{F_0^2 V_z}{\delta_{z0}} = \frac{4}{3} \left( \frac{5}{4} \right)^{4/5} \pi^{-1/5} \rho_s^{-1/5} E^{*6/5} m V_z^{13/5}. \quad (\text{A9})$$

1056 Finally, inserting equation (A9) into equation (A8) we obtain the analytical expression of  
 1057 the radiated elastic energy  $W_{el}$  on thick blocks:

$$1058 \quad W_{el} = a_2 C_{block} m V_z^{13/5}, \quad (\text{A10})$$

1059 with the coefficient  $a_2 \approx 15.93 \xi^4 \beta E^{*6/5} / (\rho_p \rho_s^{1/5} c_p^3)$ .

## Appendix B: Cumulative Distribution of Energy

1060 In this Appendix, we show how the radiated elastic energy radiated by impacts is  
 1061 distributed over the frequencies.

1062 The cumulative distribution of the radiated elastic energy shows that impacts generate  
 1063 signals with higher frequencies as the bead diameter  $d$  decreases, regardless of the structure  
 1064 (Figure 18). It is clear that the sensors used in our experiments do not measure energy for  
 1065 frequencies higher than 50 kHz. This is not a problem for impacts on the PMMA plate  
 1066 and for beads of diameter  $d$  larger than 5 mm because all of the radiated elastic energy is  
 1067 in theory below 50 kHz (Figure 18a). However, for impacts of beads of 1 mm in diameter  
 1068 on glass, concrete and marble, more than 50% of the energy is for frequencies higher than  
 1069 50 kHz (Figures 18b to 18d). Some of the radiated energy may not be measured for the  
 1070 smallest beads investigated. Note that for experiments on the glass plate and on the  
 1071 concrete and marble blocks, the profile of the cumulative energy is steep and saturates

1072 to a given frequency  $f \approx 38$  kHz,  $f \approx 30$  kHz and  $f \approx 40$  kHz, respectively, as the bead  
 1073 diameter  $d$  decreases (Figures 18b to 18d).

### Appendix C: Influence of the Impactor Shape on the Energy Budget

1074 In this Appendix, we investigate the energy budget of impacts of gravels on the glass  
 1075 plate.

1076 When a spherical bead is dropped without initially speed and rotation on a smooth sur-  
 1077 face it rebounds almost vertically and without spin. In contrast, a rough gravel rebounds  
 1078 to a much smaller height and can reach a large horizontal distance  $x$  with a high rotation  
 1079 speed  $\omega_r$  up to about  $400 \text{ rad s}^{-1}$ , depending on the face it lands on (Figure 19a). For these  
 1080 complex impactors, the kinetic energy converted in translational and rotational modes is  
 1081 therefore not negligible. The translational kinetic energy of rebound is  $E'_c = \frac{1}{2}mV'^2$  where  
 1082  $V' = V'_x\mathbf{u}_x + V'_z\mathbf{u}_z$  is the rebound speed in the cartesian frame  $(0, \mathbf{u}_x, \mathbf{u}_z)$ .  $V'_x \approx 0 \text{ cm s}^{-1}$   
 1083 for spherical beads but varies from  $5 \text{ cm s}^{-1}$  to  $40 \text{ cm s}^{-1}$  for gravels. The rotation energy  
 1084 is  $E_\omega = \frac{1}{2}I\omega_r^2$ , where  $I$  is the moment of inertia of the gravel, given by  $I = \frac{2}{5}mR^2$  if we  
 1085 assume that the gravel is spherical with an equivalent radius  $R$ . From camera recordings,  
 1086 we estimate that  $32\% \pm 17\%$  of the impact energy  $E_c$  is converted into translational energy  
 1087 of rebound  $E'_c$  and that  $13\% \pm 11\%$  is converted into rotational energy  $E_\omega$ . Regardless of  
 1088 the shape and mass  $m$  of the gravel, less energy is converted into translational energy  $E'_c$   
 1089 as its rotates faster after the impact (Figure 19b). The percentage of energy radiated in  
 1090 elastic waves  $W_{el}/E_c$  is  $3.3\% \pm 1.8\%$  and seems independent of the energy converted in  
 1091 translation energy  $E'_c/E_c$  or in rotational modes  $E_\omega/E_c$  (Figures 19c and 19d).

1092 In section 4.4.1, we adjusted the inelastic parameter  $D$  on the variation of the coefficient  
 1093 of restitution  $e$  to estimate the energy lost in viscoelastic dissipation (Figure 12). This

1094 is not possible for gravels because of the large dispersion in the results. As granite has  
 1095 similar elastic properties than glass, we assume that  $D$  is the same than for glass beads  
 1096 impacts on the glass plate i.e.,  $D = 80$  ns (see Table 5). Therefore, the viscoelastic  
 1097 dissipation  $W_{visc}$  for impacts of gravels on the glass plate may represent  $3.7\% \pm 1\%$  of  $E_c$ .  
 1098 The rest of the energy ( $48\% \pm 14\%$ ) is lost to deform plastically the gravel and or the  
 1099 glass plate. This is therefore the main process of energy dissipation for gravels impacts.

1100 The proportion of energy radiated in elastic waves  $W_{el}/E_c$  seems to decrease when  
 1101 more energy is lost in plastic deformation (Figure 19e), which is in agreement with the  
 1102 elasto-plastic model (Figure 2a).

#### Appendix D: Determining Impactor Momentum from Low Frequencies

1103 In some experiments on Figure 10, the estimations of  $m$  and  $V_z$  are affected because  
 1104 the highest frequencies of the generated vibration are not measured by the sensors or  
 1105 because of a resonance. The purpose of this Appendix is to show that we can use the low  
 1106 frequencies content of the signal to estimate the momentum  $mV_z$  of the impactor.

1107 For frequencies  $f \sim 0$  Hz, we assume as *Tsai at al.* [2012] that the impact duration  $T_c$   
 1108 is instantaneous relative to the frequencies of interest. The time Fourier transform  $\tilde{F}(f)$   
 1109 of the *Hertz* [1882] force  $F(t)$  then becomes constant in frequency:

$$1110 \quad \tilde{F}(f) = \int_{-\infty}^{+\infty} F(t) \exp(-ift) dt \sim \int_{-\infty}^{+\infty} F(t) dt. \quad (D1)$$

1111 where, if we normalize the force  $F(t)$  by its maximum value  $F_0$  and time  $t$  by the impact  
 1112 duration  $T_c$  and develop their respective expressions [equations (9) and (10)],

$$1113 \quad \int_{-\infty}^{+\infty} F(t) dt \approx 2mV_z. \quad (D2)$$



1114 The amplitude spectrum of the vibration acceleration can then be approximated by  
 1115 [*Aki and Richards*, 1980]:

$$1116 \quad |\tilde{A}_z(r, f \rightarrow 0)| \sim 2mV_z(2\pi f)^2 |\tilde{G}_{zz}(r, f)|. \quad (\text{D3})$$

1117 Using the expression of the Green's function  $|\tilde{G}_{zz}(r, f)|$  given by equations (3) and (4)  
 1118 on plates and blocks, respectively, we show that:

$$1119 \quad |\tilde{A}_z(r, f \rightarrow 0)| \sim af^b, \quad (\text{D4})$$

1120 with  $a \approx 0.73mV_z \frac{1}{B\sqrt{r}} \left(\frac{B}{\rho_p h}\right)^{5/8}$  and  $b = 3/4$  on plates and  $a \approx 100mV_z \frac{\xi^2}{\mu c_P} \frac{\sqrt{x_0(x_0^2-1)}}{f'_0(x_0)} \sqrt{\frac{2c_P}{\pi r}}$   
 1121 and  $b = 5/2$  on blocks.

1122 In order to determine the momentum  $mV_z$  of a steel bead of diameter 5 mm dropped  
 1123 from height 10 cm on the glass plate and on the concrete block, we adjust the power law  
 1124 (D4) with the measured spectra  $|\tilde{A}_z(r, f)|$  for frequencies  $f < 10$  kHz (Figure 20). The  
 1125 obtained momentum is  $mV_z \approx 6.9 \cdot 10^{-4}$  kg m s<sup>-1</sup> on glass plate and  $mV_z \approx 6.33 \cdot 10^{-4}$   
 1126 kg m s<sup>-1</sup> on the concrete block, which is in good agreement with the real momentum  
 1127  $mV_z \approx 6.85 \cdot 10^{-4}$  kg m s<sup>-1</sup>. Finally, if either  $m$  or  $V_z$  is known, this method can be used  
 1128 to estimate the other parameter.

## Notation

$c_P, c_R$	Compressional and Rayleigh waves speed
	(m s <sup>-1</sup> )
$D$	Viscoelastic coeffi- cient (s)
$d, R$	Bead diameter and radius (m)

$E_c$	Initial kinetic en- ergy (J)
$E_s, E_p, \nu_s, \nu_p$	Young's moduli (Pa) and Poisson's coef- ficients of the sphere and the plane
$E^*$	Equivalent Young's modulus (Pa)
$e$	Coefficient of resti- tution (-)
$\mathbf{F}, F_z$	Force and normal force (N)
$F_0, P_0$	Maximum force and stress of elastic im- pact (N; Pa)
$F_{max}, \delta_{max}$	Maximum force and penetration depth of inelastic impact (N)
$f, \omega$	Frequency and an- gular frequency ( $s^{-1}$ )
$f_{peak}, f_{mean}, \Delta f$	Peak, mean fre- quencies and band- width (Hz)
$g$	Acceleration of grav- itation ( $m\ s^{-2}$ )
$H$	Height of fall (m)

$h$	Plate thickness (m)
$K$	Parameter in <i>Hertz</i>
	[1882]'s theory
$k$	Wave number ( $\text{m}^{-1}$ )
$V$	Volume ( $\text{m}^3$ )
$m$	Mass (kg)
$r$	Distance from the impact (m)
$T_c$	Impact duration (s)
$t$	Time (s)
$\mathbf{u}_i$	Normalized vector of the direction $i$
$v_i, a_i$	Vibration speed and acceleration in the direction $\mathbf{u}_i$ (m $\text{s}^{-1}$ ; $\text{m s}^{-2}$ )
$\tilde{V}_i, \tilde{A}_i$	Time Fourier trans- form of $v_i$ and $a_i$ , respectively (m; m $\text{s}^{-1}$ )
$V_z, V'$	Impact speed and speed after rebound ( $\text{m s}^{-1}$ )
$v_g, v_\phi$	Group and phase velocities ( $\text{m s}^{-1}$ )

$W_{el}, \Delta E_c$	Radiated elastic energy and total energy lost (J)
$W_{el}^{th}, W_{el}^{th'}$	Theoretical radiated elastic energy predicted by <i>Hertz</i> [1882]’s and <i>Zener</i> [1941]’s models (J)
$W_{visc}, W_{other}, E'_c, E_\omega$	Energy lost in viscoelastic dissipation, in other processes, kinetic energy of rebound and rotation (J)
$x, y, z$	Coordinates in the cylindric reference frame of the block (m)
$Y_d, P_d$	Dynamic yield stress and dynamic yield strength (Pa)
$\alpha$	Viscoelastic parameter (-)

$\beta, \xi, C_{plate}, C_{block}, C_{visc}$	Coefficients involved in energy calculation (-)
$\gamma$	Attenuation coefficient of energy with distance ( $m^{-1}$ )
$\delta_z, \delta_{z0}$	Penetration depth and maximum of this depth during the impact (m)
$\lambda_Z$	Zener [1941]'s parameter (-)
$\rho_s, \rho_p$	Densities of the sphere and the plane ( $kg\ m^3$ )
$\tau$	Characteristic time of energy attenuation within the structure (s)
$\chi, \eta$	Bulk and shear viscosities (Pa s)
$\omega_r$	Rotation speed (rad $s^{-1}$ )

1129 **Acknowledgments.** We thank E. Falcon, A. Valance, Y. Forterre, D. Royer, A. Schub-  
 1130 nel, T. Reuschlé and L. Jouniaux for helpful discussions. We are indebted to A. Steyer for  
 1131 technical help. We thank Aude Nachbaur, Hiromi Kobayashi, Christophe Rivière, Em-

1132 manuel Des Garets and Emilie Nowak for assistance in rockfall experiments in Tahiti. We  
1133 are grateful to Florent Gimbert and an anonymous reviewer for their interesting comments  
1134 to our initial manuscript. This work was supported by the european project ERC SLID-  
1135 EARTHQUAKES and the Agence Nationale de la Recherche ANR LANDQUAKES, REALISE  
1136 and ITN FLOWTRANS.

## References

- 1137 Aki, K., and P. Richards (1980), *Quantitative Seismology : Theory and Methods*, vol. 1,  
1138 W.H. Freeman.
- 1139 Allstadt, K. (2013), Extracting source characteristics and dynamics of the August 2010  
1140 Mount Meager landslide from broadband seismograms, *J. Geophys. Res.*, *118*(3), doi:  
1141 10.1002/jgrf.20110.
- 1142 Andreotti, B., Y. Forterre, and O. Pouliquen (2013), *Granular Media: Between Fluid and*  
1143 *Solid*, vol. 1, Cambridge Univ. Press.
- 1144 Brilliantov, N. V., F. Spahn, J.-M. Hertzsch, and T. Pöschel (1996), Model for collisions  
1145 in granular gases, *Phys. Rev. E*, *53*, 5382–5392, doi:10.1103/PhysRevE.53.5382.
- 1146 Burtin, A., L. Bollinger, J. Vergne, R. Cattin, and J. L. Nábělek (2008), Spectral  
1147 analysis of seismic noise induced by rivers: A new tool to monitor spatiotempo-  
1148 ral changes in stream hydrodynamics, *J. Geophys. Res.*, *113*(B5), B05,301, doi:  
1149 10.1029/2007JB005034.
- 1150 Buttle, D. J., and C. B. Scruby (1990), Characterization of particle impact by quantitative  
1151 acoustic emission, *Wear*, *137*(1), 63–90, doi:10.1016/0043-1648(90)90018-6.

- 1152 Buttle, D. J., S. R. Martin, and C. B. Scruby (1991), Particle sizing by quantitative  
1153 acoustic emission, *Res. Nondestruct. Eval.*, *3*(1), 1–26, doi:10.1007/BF01606508.
- 1154 Crook, A. W. (1952), A study of some impacts between metal bodies by a piezo–lectric  
1155 method, *Philos. T. Roy. Soc. A*, *212*(1110), 377–390, doi:10.1098/rspa.1952.0088.
- 1156 Dammeier, F., J. R. Moore, F. Haslinger, and S. Loew (2011), Characterization of alpine  
1157 rockslides using statistical analysis of seismic signals, *J. Geophys. Res.*, *116*(F4), doi:  
1158 10.1029/2011JF002037.
- 1159 Davies, R. M. (1949), The determination of static and dynamic yield stresses using a steel  
1160 ball, *P. Roy. Soc. Lond. A Mat.*, *197*(1050), 416–432, doi:10.1098/rspa.1949.0073.
- 1161 Deparis, J., D. Jongmans, F. Cotton, L. Baillet, F. Thouvenot, and D. Hantz (2008),  
1162 Analysis of rock-fall and rock-fall avalanche seismograms in the French Alps, *Bull.*  
1163 *Seism. Soc. Am.*, *98*(4), 1781–1796, doi:10.1785/0120070082.
- 1164 Dewez, T. J. B., A. Nachbaur, C. Mathon, O. Sedan, H. Kobayashi, C. Rivire, F. Berger,  
1165 E. Des Garets, and E. Nowak (2010), OFAI: 3D block tracking in a real-size rock-  
1166 fall experiment on a weathered volcanic rocks slope of Tahiti, French Polynesia, *Conf.*  
1167 *Proceedings, Rock Slope Stability 2010, 24–25 nov. 2010, Paris, France*, pp. 1–13.
- 1168 Duran, J. (2010), *Sands, powders and grains: an introduction to the physics of granular*  
1169 *materials*, Boston Academic Press.
- 1170 Falcon, E., C. Laroche, S. Fauve, and C. Coste (1998), Behavior of one inelastic ball bounc-  
1171 ing repeatedly off the ground, *Eur. Phys. J. B*, *3*(1), 45–57, doi:10.1007/s100510050283.
- 1172 Farin, M. (2015), Études expérimentales de la dynamique et de l’émission sismique des  
1173 instabilités gravitaires, Ph.D. thesis, IPGP, Paris.

- 1174 Farin, M., A. Mangeney, J. de Rosny, R. Toussaint, J. Sainte-Marie, and N. Shapiro  
1175 (2015), Experimental validation of theoretical methods to estimate the energy radiated  
1176 by elastic waves during an impact, (*submitted*).
- 1177 Favreau, P., A. Mangeney, A. Lucas, G. Crosta, and F. Bouchut (2010), Numerical mod-  
1178 eling of landquakes, *Geophys. Res. Let.*, *37*, doi:10.1029/2010GL043512.
- 1179 Ferrazzini, V., and K. Aki (1992), *Volcanic Seismology: Preliminary Results from a Field*  
1180 *Experiment on Volcanic Events at Kilauea Using an Array of Digital Seismographs*,  
1181 168–189 pp., Springer-Verlag Berlin.
- 1182 Geotechdata.info (2013), Soil young’s modulus, [http://www.geotechdata.info/parameter/soil-](http://www.geotechdata.info/parameter/soil-young%27s-modulus.html)  
1183 [young%27s-modulus.html](http://www.geotechdata.info/parameter/soil-young%27s-modulus.html), accessed: 2015-20-04.
- 1184 Gimbert, F., V. C. Tsai, and M. P. Lamb (2014), A physical model for seismic noise  
1185 generation by turbulent flow in rivers, *J. Geophys. Res. Earth Surf.*, *119*, 2209–2238,  
1186 doi:10.1002/2014JF003201.
- 1187 Goyder, H., and R. G. White (1980), Vibrational power flow from machines into built-  
1188 up structures, part I: introduction and approximate analyses of beam and plate-like  
1189 foundations, *J. Sound Vib.*, *68*(1), 59–75, doi:10.1016/0022-460X(80)90452-6.
- 1190 Helmstetter, A., and S. Garambois (2010), Seismic monitoring of Séchilienne rockslide  
1191 (French Alps): Analysis of seismic signals and their correlation with rainfalls, *J. Geo-*  
1192 *phys. Res.*, *115*(F3), F03,016, doi:10.1029/2009JF001532.
- 1193 Hertz, H. (1882), Über die Berührung fester elastischer Körper (On the vibration of solid  
1194 elastic bodies), *J. Reine Angew. Math.*, *92*, 156–171, doi:10.1515/crll.1882.92.156.
- 1195 Hertzsch, J., F. Spahn, and N. V. Brilliantov (1995), On low-velocity collisions of vis-  
1196 coelastic particles, *J. Phys. II France*, *5*(11), 1725–1738, doi:10.1051/jp2:1995210.



- 1197 Hibert, C., A. Mangeney, G. Grandjean, and N. M. Shapiro (2011), Slope instabilities  
1198 in Dolomieu crater, Réunion Island: From seismic signals to rockfall characteristics, *J.*  
1199 *Geophys. Res.*, *116*(F4), F04,032, doi:10.1029/2011JF002038.
- 1200 Hibert, C., A. Mangeney, G. Grandjean, C. Baillard, D. Rivet, N. M. Shapiro, C. Satriano,  
1201 A. Maggi, P. Boissier, V. Ferrazzini, and W. Crawford (2014a), Automated identifica-  
1202 tion, location, and volume estimation of rockfalls at piton de la fournaise volcano, *J.*  
1203 *Geophys. Res.*, *119*(5), 1082–1105, doi:10.1002/2013JF002970.
- 1204 Hibert, C., G. Ekström, and C. Stark (2014b), Dynamics of the Bingham  
1205 Canyon Mine landslides from seismic signal analysis, *Geophys. Res. Let.*, *41*, doi:  
1206 10.1002/2014GL060592.
- 1207 Hunter, S. C. (1957), Energy absorbed by elastic waves during impact, *J. Mech. Phys.*  
1208 *Solids*, *5*(3), 162–171, doi:10.1016/0022-5096(57)90002-9.
- 1209 Israelachvili, J. (2002), *Intermolecular and surface forces: third edition*, Springer Verlag,  
1210 New York.
- 1211 Johnson, K. (1985), *Contact Mechanics*, Cambridge University Press.
- 1212 Kanamori, H., and J. W. Given (1982), Analysis of long-period seismic waves excited by  
1213 the May 18, 1980, eruption of Mount St. Helens – A terrestrial monopole, *J. Geophys.*  
1214 *Res.*, *87*, 5422–5432, doi:10.1029/JB087iB07p05422.
- 1215 Kuwabara, G., and K. Kono (1987), Restitution coefficient in a collision between two  
1216 spheres, *Jpn. J. Appl. Phys.*, *26*(8R), 1230.
- 1217 Lévy, C., A. Mangeney, F. Bonilla, C. Hibert, E. Calder, P. Smith, and P. Cole (2015),  
1218 Friction weakening in granular flows deduced from seismic records at the Souffrière Hills  
1219 Volcano, Montserrat, (*submitted*).

- 1220 Mayeda, K., and L. Malagnini (2010), Source radiation invariant property of local and  
1221 near-regional shear-wave coda: Application to source scaling for the Mw 5.9 Wells,  
1222 Nevada sequence, *Geophys. Res. Lett.*, *37*(7), doi:10.1029/2009GL042148.
- 1223 McLaskey, G. C., and S. D. Glaser (2010), Hertzian impact: Experimental study of  
1224 the force pulse and resulting stress waves, *J. Acoust. Soc. Am.*, *128*(3), 1087, doi:  
1225 10.1121/1.3466847.
- 1226 Miller, G. F., and H. Pursey (1954), The field and radiation impedance of mechanical  
1227 radiators on the free surface of a semi-infinite isotropic solid, *Proc. R. Soc. Lond. A.*  
1228 *Mat.*, *223*(1155), 521–541, doi:10.1098/rspa.1954.0134.
- 1229 Miller, G. F., and H. Pursey (1955), On the partition of energy between elastic  
1230 waves in a semi-infinite solid, *Proc. R. Soc. Lond. A. Mat.*, *233*(1192), 55–69, doi:  
1231 10.1098/rspa.1955.0245.
- 1232 Moretti, L., A. Mangeney, Y. Capdeville, E. Stutzmann, C. Huggel, D. Schneider, and  
1233 F. Bouchut (2012), Numerical modeling of the Mount Steller landslide flow history  
1234 and of the generated long period seismic waves, *Geophys. Res. Lett.*, *39*(16), doi:  
1235 10.1029/2012GL052511.
- 1236 Moretti, L., K. Allstadt, A. Mangeney, Y. Capdeville, E. Stutzmann, and F. Bouchut  
1237 (2015), Numerical modeling of the Mount Meager landslide constrained by its force  
1238 history derived from seismic data, *J. Geophys. Res.: Solid Earth*, *120*(4).
- 1239 Norris, R. D. (1994), Seismicity of rockfalls and avalanches at three cascade range vol-  
1240 canoes: Implications for seismic detection of hazardous mass movements, *Bull. Seism.*  
1241 *Soc. Am.*, *84*(6), 1925–1939.

- 1242 Ramírez, R., T. Pöschel, N. V. Brilliantov, and T. Schwager (1999), Coefficient of  
1243 restitution of colliding viscoelastic spheres, *Phys. Rev. E*, *60*(4), 4465–4472, doi:  
1244 10.1103/PhysRevE.60.4465.
- 1245 Reed, J. (1985), Energy losses due to elastic wave propagation during an elastic impact,  
1246 *J. Phys. D Appl. Phys.*, *18*(12), 2329, doi:10.1088/0022-3727/18/12/004.
- 1247 Royer, D., and E. Dieulesaint (2000), *Elastic Waves in Solids I: Free and Guided Propa-*  
1248 *gation*, Springer.
- 1249 Sánchez-Sesma, F. J., R. L. Weaver, H. Kawase, S. Matsushima, F. Luzon, and  
1250 M. Campillo (2011), Energy Partitions among Elastic Waves for Dynamic Surface  
1251 Loads in a Semi-Infinite Solid, *Bull. Seism. Soc. Am.*, *101*(4), 1704–1709, doi:  
1252 10.1785/0120100196.
- 1253 Schmandt, B., R. C. Aster, D. Scherler, V. C. Tsai, and K. Karlstrom (2013), Multiple  
1254 fluvial processes detected by riverside seismic and infrasound monitoring of a controlled  
1255 flood in the Grand Canyon, *Geophys. Res. Lett.*, *40*, 4858–4863, doi:10.1002/grl.50953.
- 1256 Suriñach, E., I. Vilajosana, G. Khazaradze, B. Biescas, G. Furdada, and J. M. Vilaplana  
1257 (2005), Seismic detection and characterization of landslides and other mass movements,  
1258 *Nat. Hazards Earth Syst. Sci.*, *5*(6), 791–798, doi:10.5194/nhess-5-791-2005.
- 1259 The Engineering Toolbox (2014), Concrete properties, < *http* :  
1260 *//www.engineeringtoolbox.com/concrete - properties - d\_1223.html* >, accessed:  
1261 11-20-14.
- 1262 Tillett, J. (1954), A study of the impact of spheres on plates, *Proc. Phys. Soc. B*, *67*(9),  
1263 677, doi:10.1088/0370-1301/67/9/304.

- 1264 Troccaz, P., R. Woodcock, and F. Laville (2000), Acoustic radiation due to the inelas-  
1265 tic impact of a sphere on a rectangular plate, *J. Acoust. Soc. Am.*, *108*, 2197, doi:  
1266 10.1121/1.1312358.
- 1267 Tsai, V. C., B. Minchew, M. P. Lamb, and J.-P. Ampuero (2012), A physical model for  
1268 seismic noise generation from sediment transport in rivers, *Geophys. Res. Lett.*, *39*(2),  
1269 doi:10.1029/2011GL050255.
- 1270 Vilajosana, I., E. Suriñach, A. Abellan, G. Khazaradze, D. Garcia, and J. Llosa (2008),  
1271 Rockfall induced seismic signals: case study in Montserrat, Catalonia, *Nat. Hazards*  
1272 *Earth Syst. Sci.*, *8*(4), 805–812, doi:10.5194/nhess-8-805-2008.
- 1273 Vinningland, J. L., O. Johnsen, E. G. Flekkøy, R. Toussaint, and K. J. Måløy (2007a),  
1274 Experiments and simulations of a gravitational granular flow instability, *Phys. Rev. E*,  
1275 *76*, 051,306, doi:10.1103/PhysRevE.76.051306.
- 1276 Vinningland, J. L., O. Johnsen, E. G. Flekkøy, R. Toussaint, and K. J. Måløy (2007b),  
1277 Granular rayleigh-taylor instability: Experiments and simulations, *Phys. Rev. Lett.*, *99*,  
1278 048,001, doi:10.1103/PhysRevLett.99.048001.
- 1279 Weaver, R. L. (1985), Diffuse elastic waves at a free surface, *J. Acoust. Soc. Am.*, *78*,  
1280 doi:10.1121/1.392576.
- 1281 Yamada, M., Y. Matsushi, M. Chigira, and J. Mori (2012), Seismic recordings of land-  
1282 slides caused by Typhoon Talas (2011), Japan, *Geophys. Res. Lett.*, *39*(13), doi:  
1283 10.1029/2012GL052174.
- 1284 Zener, C. (1941), The intrinsic inelasticity of large plates, *Phys. Rev.*, *59*, 669–673, doi:  
1285 10.1103/PhysRev.59.669.

**Table 1.** Scaling laws for the radiated elastic energy and the energy dissipated in viscoelasticity<sup>a</sup>

	Plates	Blocks
$W_{el}$	$a_1 C_{plate} m^{5/3} V_z^{11/5}$ $a_3 C_{plate} R^5 H^{11/10}$	$a_2 C_{block} m V_z^{13/5}$ $a_4 C_{block} R^3 H^{13/10}$
$W_{visc}$	$C_{visc} m V_z^2$ $a_5 C_{visc} R^3 H$	
	$a_1 \approx 0.18 \frac{E^{*2/5}}{\rho_s^{1/15} \sqrt{B \rho_p h}}$	$a_2 \approx 15.93 \frac{\xi^4 \beta E^{*6/5}}{\rho_p \rho_s^{1/5} c_p^3}$
	$a_3 = (2g)^{11/10} (\frac{4}{3} \pi \rho_s)^{5/3} a_1$	$a_4 = (2g)^{13/10} \frac{4}{3} \pi \rho_s a_2$
	$a_5 = 2g \frac{4}{3} \pi \rho_s$	

<sup>a</sup> Radiated elastic energy  $W_{el}$  and energy  $W_{visc}$  dissipated in viscoelasticity for plates of thickness  $h$  and blocks as a function of the impact parameters. The coefficients  $a_i$  depend only on the elastic parameters of the impactor and of the structure. The parameter  $\beta$  is a function of the Poisson's ratio  $\nu_p$  only (see Figure 17 of Appendix A). The coefficients  $C_{plate}$  and  $C_{block}$  are represented on Figure 2.

**Table 2.** Characteristics frequencies<sup>a</sup>

	$f_{mean}$	$\Delta f$
plates	$0.75/T_c$	$0.72/T_c$
blocks	$1/T_c$	$0.6/T_c$

<sup>a</sup> Theoretical mean frequency  $f_{mean}$  and bandwidth  $\Delta f$ , as respectively defined by equations (25) and (26), of the acoustic signal generated by an elastic impact on a thin plate and on a thick block.

**Table 3.** Characteristics of the impactors used in experiments: density  $\rho_s$ , Young's modulus  $E_s$ , Poisson's ratio  $\nu_s$ , diameter  $d$  and mass  $m$ .

	material	$\rho_s$ (kg m <sup>-3</sup> )	$E_s$ (GPa)	$\nu_s$ -	$d$ (mm)	$m$ (g)
spherical beads	glass	2500	74	0.2	1 – 20	$1.3 \cdot 10^{-3} - 10$
	polyamide	1140	4	0.4	2 – 20	$6 \cdot 10^{-4} - 4.8$
	steel	7800	203	0.3	1 – 20	$4.1 \cdot 10^{-3} - 33$
gravels	granite	3600	60	0.27	$\approx 4 - 28$	$0.08 - 18$

**Table 4.** Characteristics of the materials used in experiments<sup>a</sup>

material		$\rho_p$ (kg m <sup>-3</sup> )	$E_p$ (GPa)	$\nu_p$ -	$\gamma$ (1/m)	$\tau$ (s)	$v_g$ (m s <sup>-1</sup> )	$v_\phi$ (m s <sup>-1</sup> )
glass	$kh < 1$	2500	74	0.2	$0.014f^{1/6}$	$3.8f^{-2/3}$	$18.6f^{1/2}$	$9.3f^{1/2}$
	$kh > 1$				$8.5 \times 10^{-5}f^{2/3}$		3100	3100
PMMA	$kh < 1$	1180	2.4	0.37	1	$0.09f^{-1/2}$	$11.7f^{1/2}$	$5.8f^{1/2}$
	$kh > 1$				$4.8 \times 10^{-3}f^{2/3}$	$0.15f^{-2/3}$	1400	1400
concrete	-	2300	16.3	0.4	$2.3 \cdot 10^{-5}f$	$28f^{-1}$	1530	1530
marble	-	2800	26	0.3	$2.5 \cdot 10^{-5}f$	$23.1f^{-1}$	1750	1750

<sup>a</sup> Density  $\rho_p$ , Young's modulus  $E_p$ , Poisson's ratio  $\nu_p$ , characteristic distance  $1/\gamma$  and time  $\tau$  of energy attenuation, group velocity  $v_g$  and phase velocity  $v_\phi$  (that depend on the frequency  $f$  (in Hz)) [see the supplementary materials of *Farin et al.*, 2015, for details on the measurement of  $\gamma$  and  $\tau$ ].

**Table 5.** Viscoelastic constant  $D$  (in ns)<sup>a</sup>

substrate		PMMA	glass	concrete	marble
bead	glass	230	80	100	180
	polyamide	580	550	300	300
	steel	190	35	200	200

<sup>a</sup> Value of the viscoelastic constant  $D$  appearing in equation (19) and adjusted on experimental data for impacts of spherical beads of different material (rows) on the different substrates (columns).

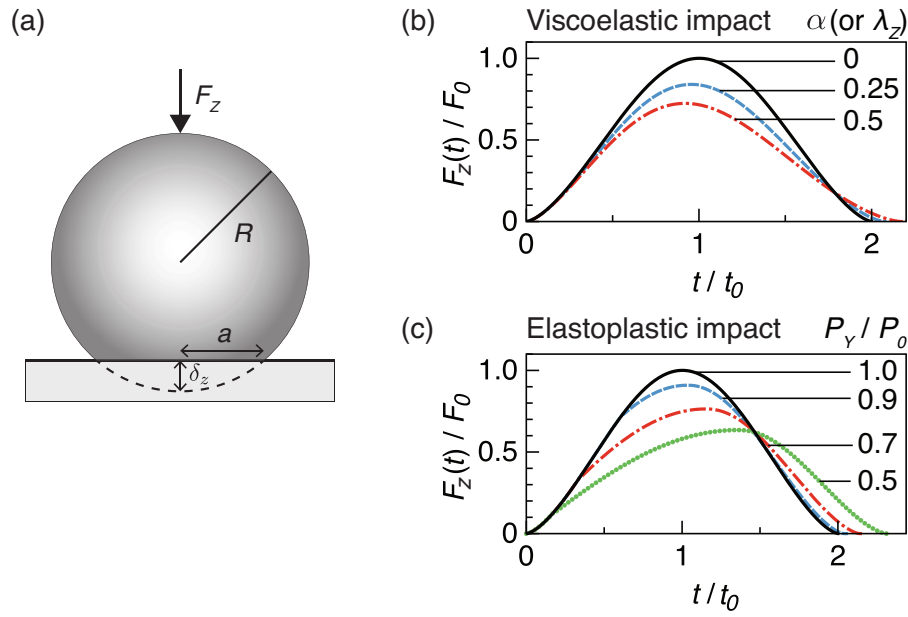


**Figure 1.** (a) Schematic showing the penetration depth  $\delta_z$  of a sphere of radius  $R$  on a plane surface during an impact. Geometrically, the surface of contact is a circle of radius  $a$ . (b) and (c) Normalized force of impact  $F_z(t/t_0)/F_0$  for (b) different values of the viscoelastic parameter  $\alpha$  (or  $\lambda_z$  for *Zener* [1941]’s theory; see section 2.1.1.2) and for (c) different values of the stresses ratio  $P_Y/P_0$ .  $F_0$  and  $t_0 = T_c/2$  are respectively the force and the time at maximal compression during an elastic impact i.e., for  $\alpha = 0$  and  $P_Y/P_0 = 1$ .

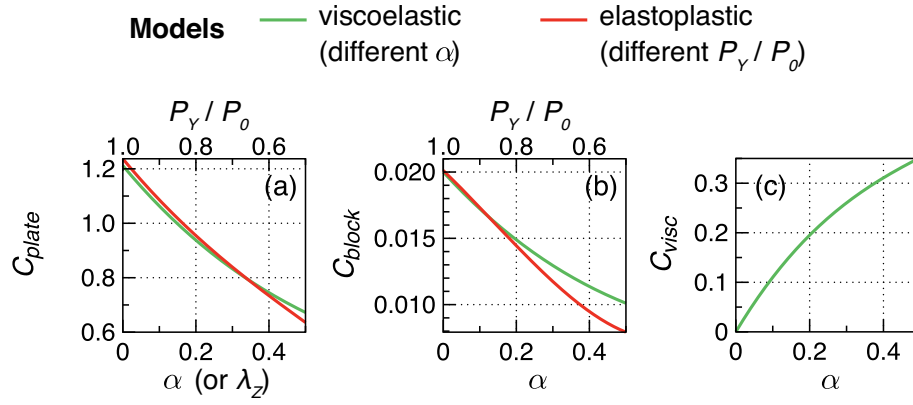


**Figure 2.** (a), (b) and (c) Values of the constants (a)  $C_{plate}$ , (b)  $C_{block}$  and (c)  $C_{visc}$  as a function of the inelastic parameters  $\alpha$  for a viscoelastic impact (or  $\lambda_Z$  for *Zener* [1941]’s theory) (green) and  $P_Y/P_0$  for an elasto-plastic impact (red).

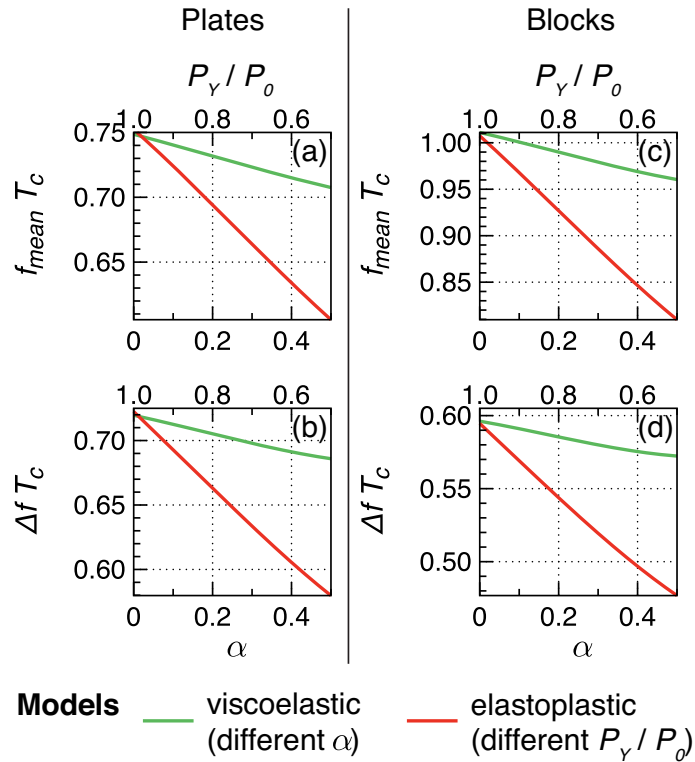


**Figure 3.** Theoretical values of the (a), (c) mean frequency  $f_{mean}$  and (b), (d) bandwidth  $\Delta f$  for (a) and (b) thin plates and (c) and (d) thick blocks, as a function of the inelastic parameters  $\alpha$  (green) and  $P_Y/P_0$  (red). All frequencies are multiplied by *Hertz* [1882]’s impact duration  $T_c$  to be dimensionless.



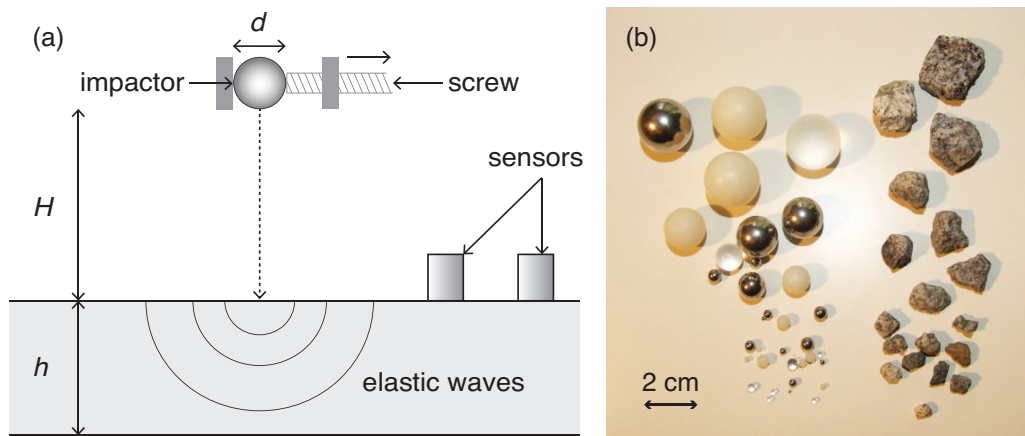


**Figure 4.** (a) Scheme of the experimental setup. An impactor of diameter  $d$  is initially held by a screw and dropped without initial speed or rotation on a hard structure of thickness  $h$ . The height of fall  $H$  varies from 2 cm to 30 cm. The impact generates elastic waves, recorded by an array of accelerometers. (b) Spherical beads of glass, polyamide and steel and granite gravels used as impactors in the experiments.

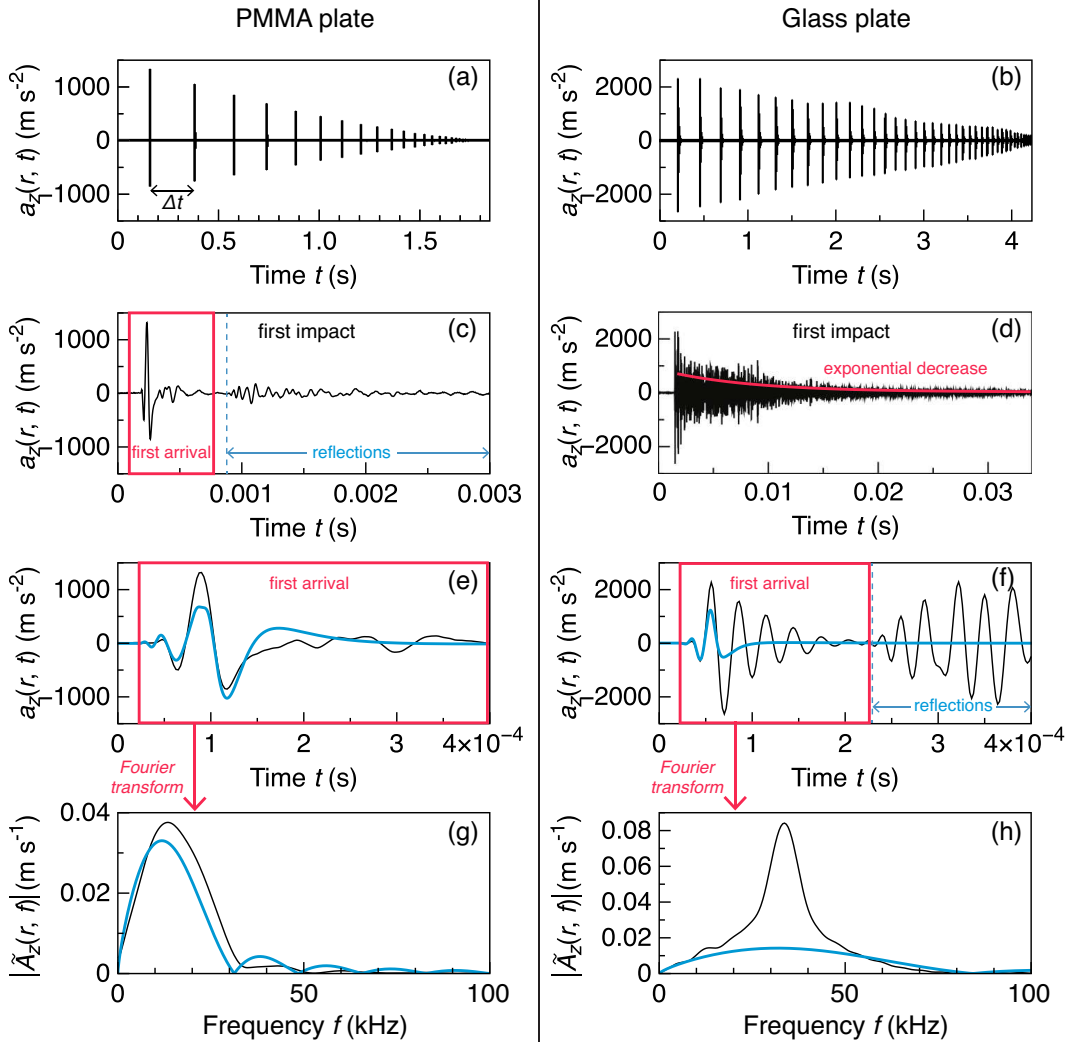


**Figure 5.** (a) and (b) Acceleration signal  $a_z(r, t)$  generated by the successive impacts of a steel bead of diameter  $d = 5$  mm, dropped from height  $H = 10$  cm on (a) the PMMA plate and (b) the glass plate. The time of flight  $\Delta t$  between two impacts is equal to the duration between two peaks. (c) and (d) Zoom on the signal of the first rebound, filtered below 100 kHz. The coda envelope decreases exponentially with time in the glass plate (red line). (c),(e) and (f) The first arrival is delimited by a red frame and the first reflections off the plate lateral sides arrive at the right of the blue dashed line. The arrival time of the reflections is computed knowing the wave speed and the distance between the sensor and the substrate sides. (g) and (h) The time Fourier transform of the first arrival gives the amplitude spectrum  $|\tilde{A}_z(r, f)|$  as a function of the frequency  $f$ . The thick blue line in Figures (e) to (h) represents the synthetic signal and amplitude spectrum obtained by September 11, 2015, [1680] pm force of impact with the Green's function.

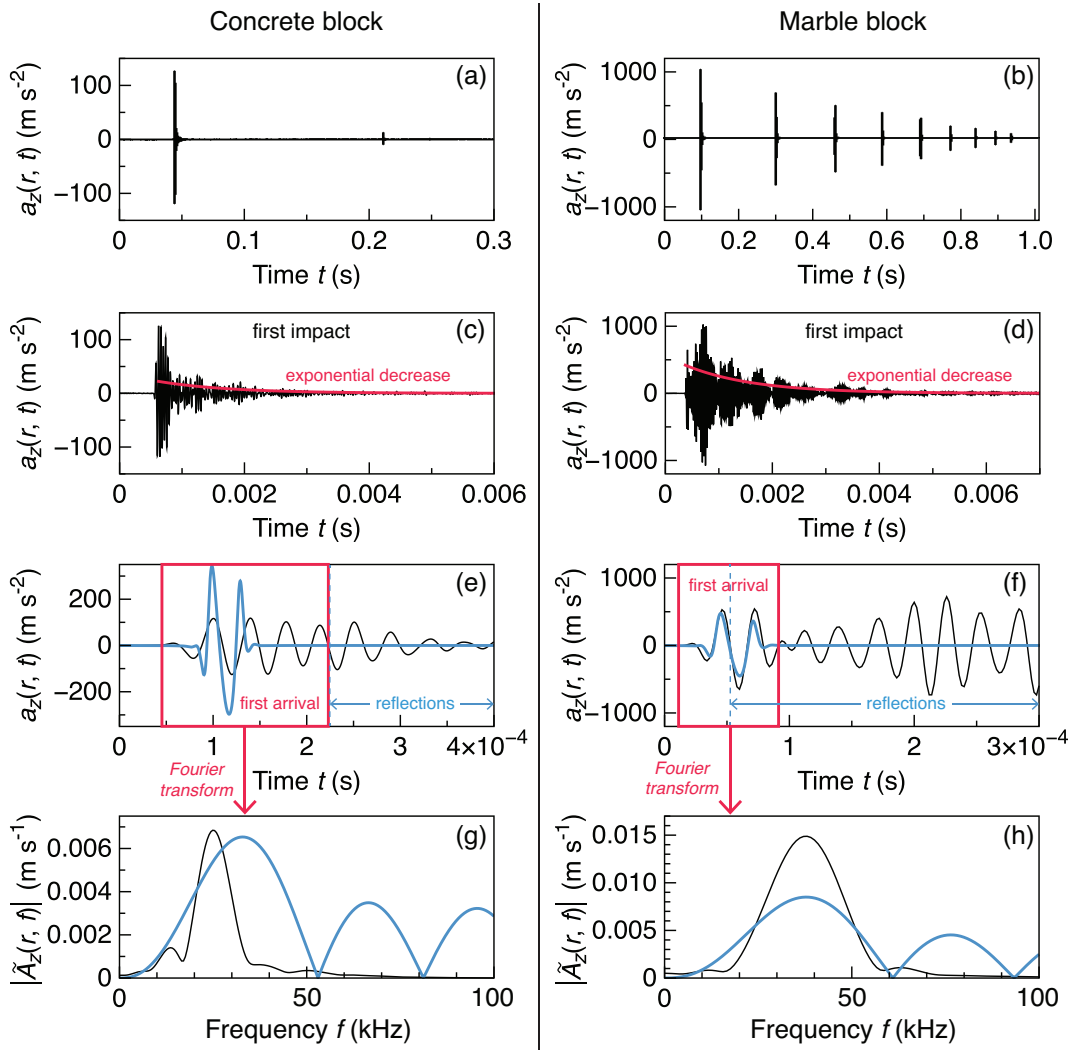


**Figure 6.** (a) and (b) Acceleration signal  $a_z(r, t)$  generated by the successive impacts of a steel bead of diameter  $d = 5$  mm, dropped from height  $H = 10$  cm on (a) the concrete block and (b) the marble block. (c) and (d) Zoom on the signal of the first rebound, filtered below 100 kHz. The coda envelope decreases exponentially with time (red line). (e) and (f) The first arrival is delimited by a red frame and the first reflections off the plate lateral sides arrive at the right of the blue dashed line. The arrival time of the reflections is computed knowing the wave speed and the distance between the sensor and the substrate sides. (g) and (h) The time Fourier transform of the first arrival gives the amplitude spectrum  $|\tilde{A}_z(r, f)|$  as a function of the frequency  $f$ . The thick blue line in Figures (e) to (h) represents the synthetic signal and amplitude spectrum obtained by convolution of *Hertz* [1882]’s force of impact with the Green’s

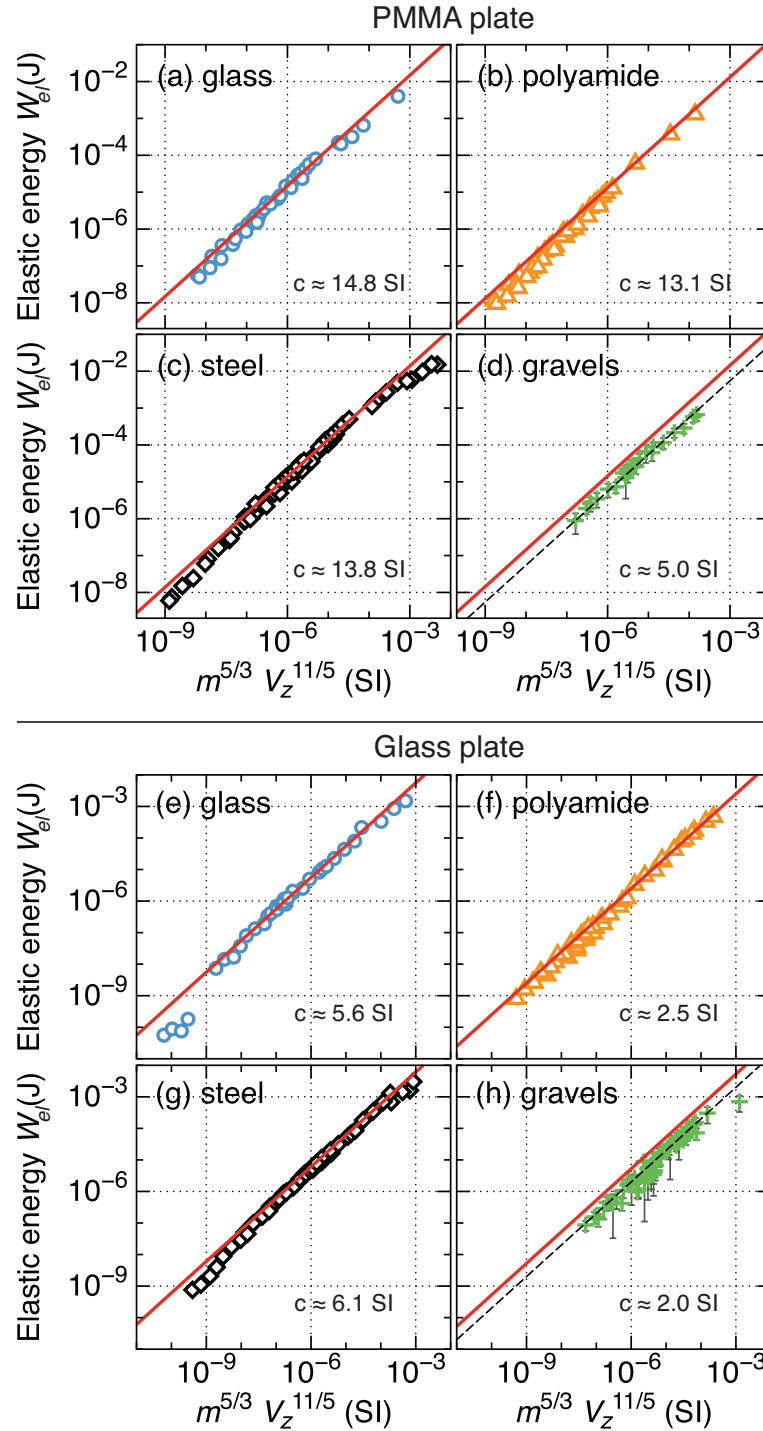


**Figure 7.** Radiated elastic energy  $W_{el}$  as a function of  $m^{5/3}V_z^{11/5}$  for impacts of (a)-(e) glass, (b)-(f) polyamide and (c)-(g) steel beads and (d)-(h) gravels on (a) to (d) the PMMA plate and on (e) to (h) the glass plate. The red line corresponds to the theoretical energy  $W_{el}^{th}$  given in Table 1 for an elastic impact i.e., with  $C_{plate} = 1.21$ . The black dashed line is a fit to the data of the law  $W_{el} = cm^{5/3}V_z^{11/5}$ , with coefficient  $c$  indicated in International System Units (SI). In most cases, this line collapses with the theoretical line in red. Error bars on  $W_{el}$  ( $\pm 35\%$ ) are computed from  $\pm 1$  standard deviation on a series of 20 experiments and are symbols sized.

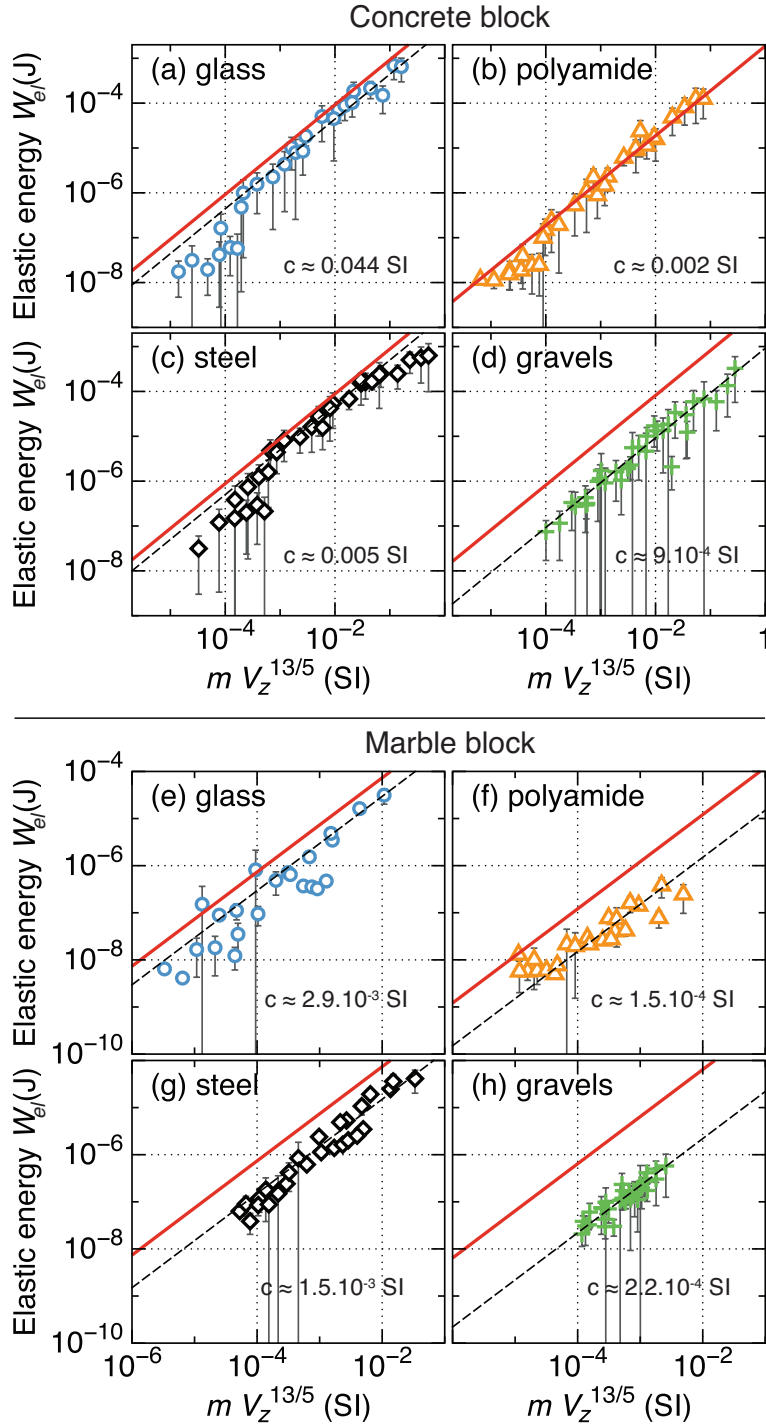


**Figure 8.** Radiated elastic energy  $W_{el}$  as a function of  $mV_z^{13/5}$  for impacts of (a)-(e) glass, (b)-(f) polyamide and (c)-(g) steel beads and (d)-(h) gravels on (a) to (d) the concrete block and on (e) to (h) the marble block. The red line corresponds to the theoretical energy  $W_{el}^{th}$  given in Table 1 for an elastic impact i.e., with  $C_{block} = 0.02$ . The black dashed line is a fit to the data of the law  $W_{el} = cmV_z^{13/5}$ , with coefficient  $c$  indicated in International System Units (SI).

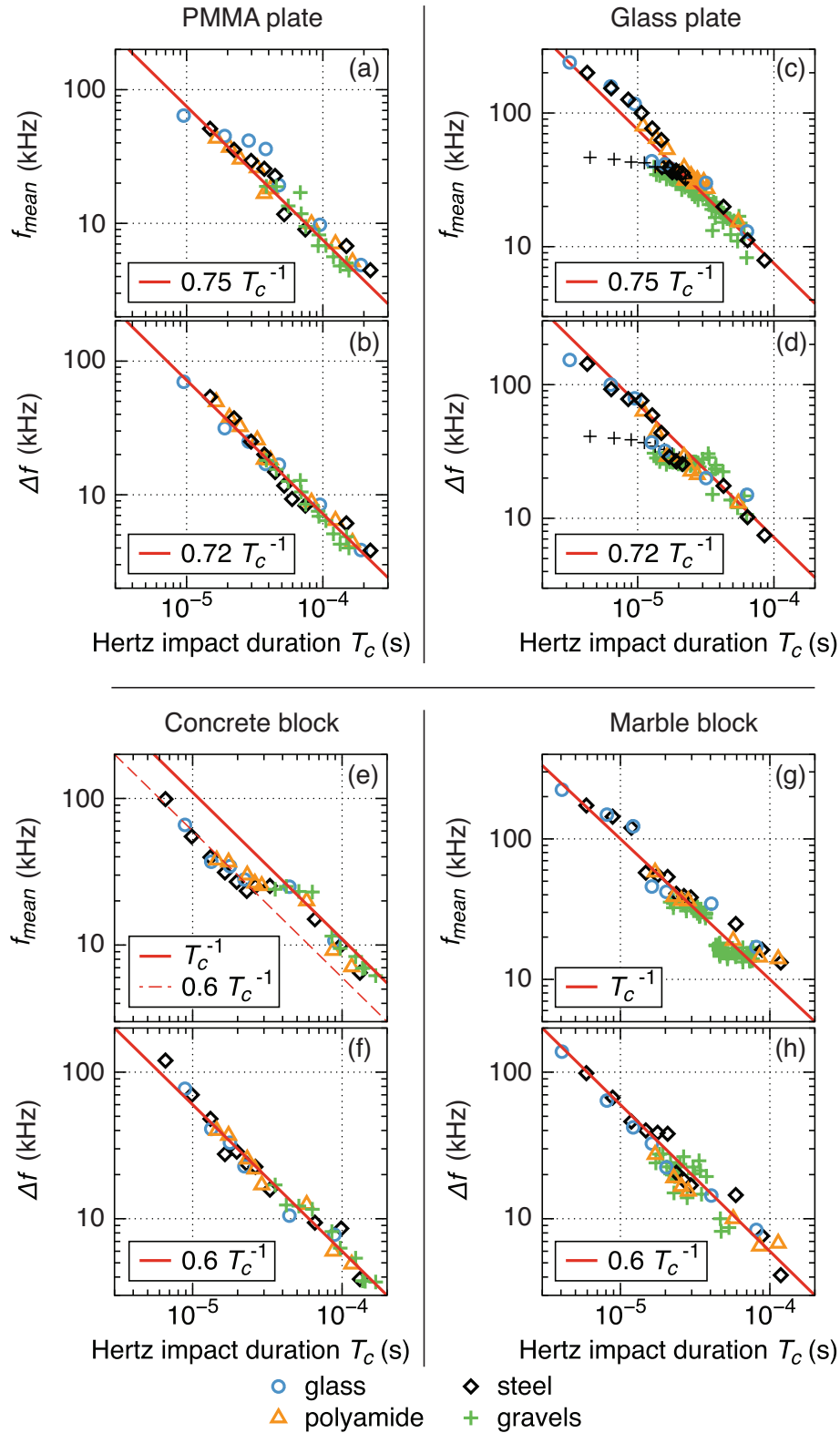


**Figure 9.** (a), (c), (e) and (g) Mean frequency  $f_{mean}$  and (b), (d), (f) and (h) bandwidth  $\Delta f$  as a function of *Hertz* [1882]’s impact duration  $T_c$  [equation (9)] for impacts of glass, polyamide and steel beads and granite gravels on (a) and (b) the PMMA plate, (c) and (d) the glass plate, (e) and (f) the concrete block and (g) and (h) the marble block. The red line corresponds to the theoretical prediction (Table 2) and the red dashed line in (e) is a fit to the data. The black crosses on Figures (c) and (d) correspond to the frequencies of the signals generated by steel beads measured with the accelerometers type 8309, that resonate around 38 kHz on the glass

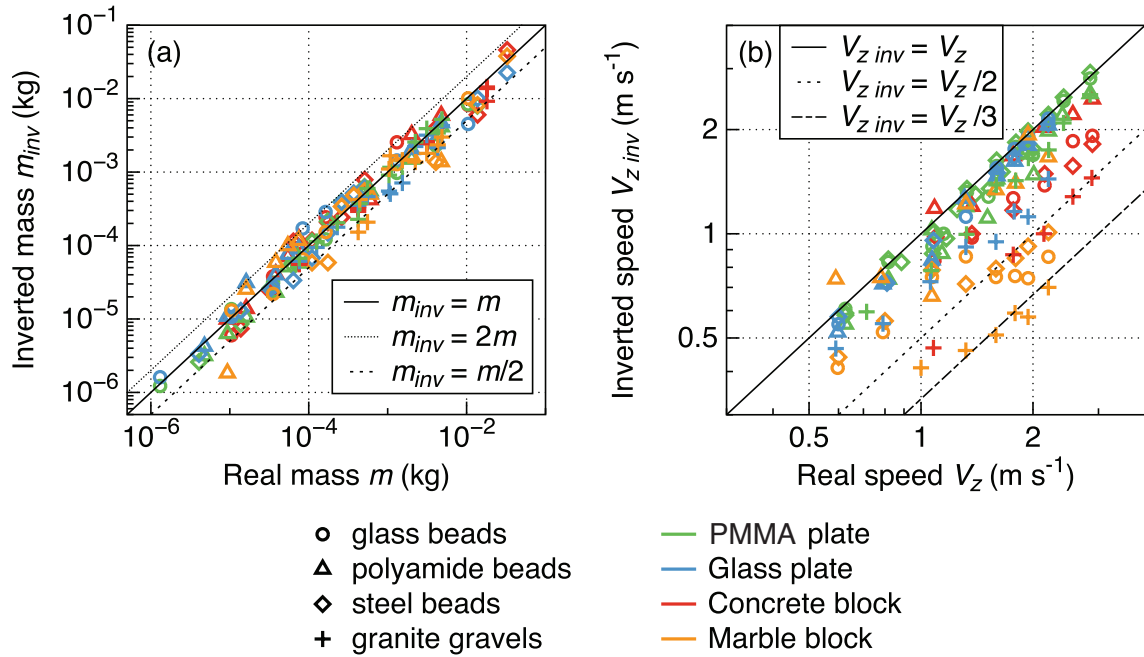


**Figure 10.** (a) Mass  $m_{inv}$  inverted from signal bandwidth  $\Delta f$  and radiated elastic energy  $W_{el}$  using equations (27) for plates and (29) for blocks as a function of the real mass  $m$ . (b) Impact speed  $V_{z\ inv}$  inverted using equations (28) for plates and (30) for blocks as a function of the real impact speed  $V_z$ . The black full line is a perfect fit.

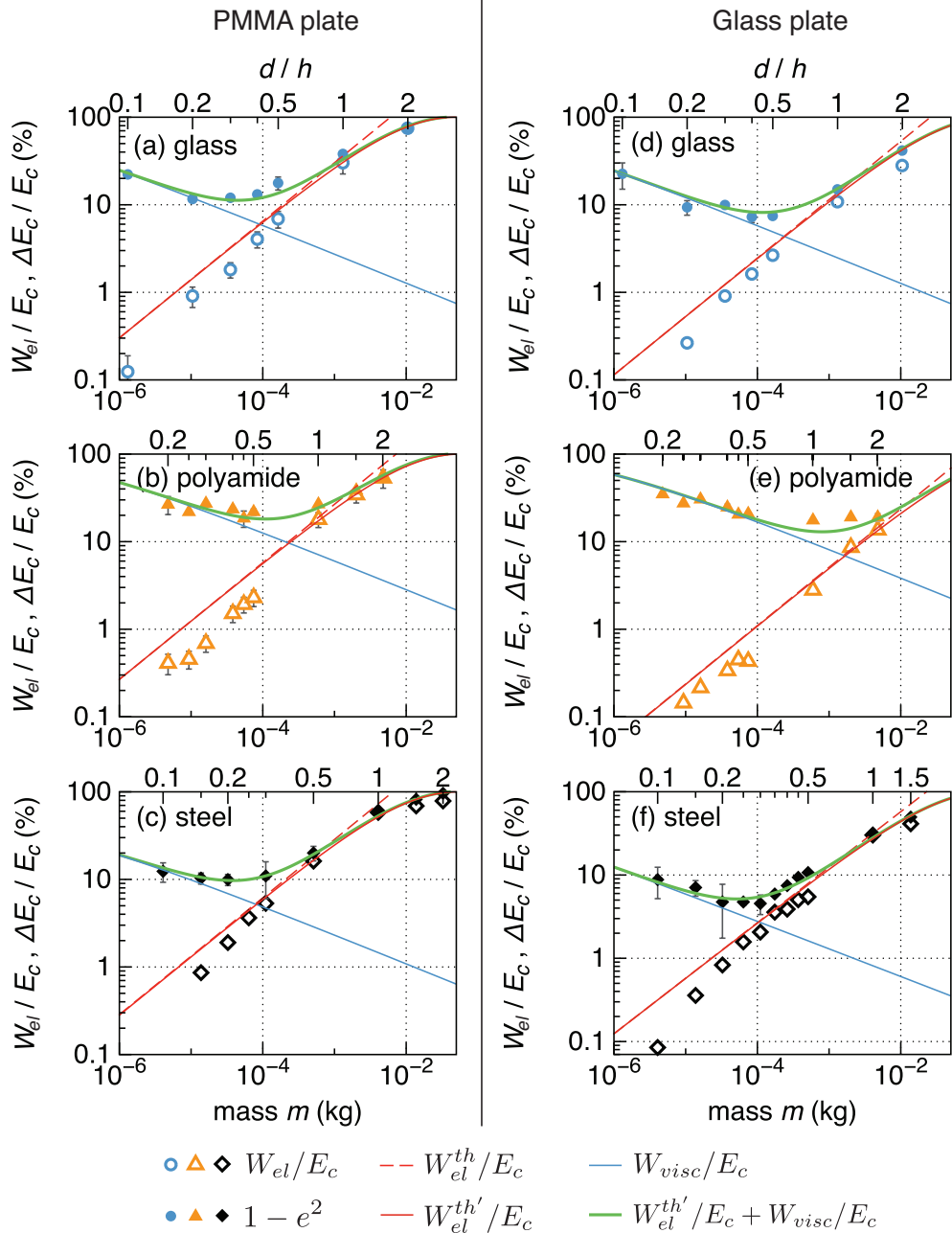


**Figure 11.** Ratio of the measured radiated elastic energy  $W_{el}$  over the impact energy  $E_c = \frac{1}{2}mV_z^2$  (empty symbols) and measured lost energy ratio  $\Delta E_c/E_c = 1 - e^2$  (full symbols) as a function of bead mass  $m$  and of the ratio of the bead diameter  $d$  on the plate thickness  $h$  for impacts of (a)-(d) glass, (b)-(e) polyamide and (c)-(f) steel beads on (a) to (c) the PMMA plate and on (d) to (f) the glass plate. The red dashed line corresponds to the theoretical ratio  $W_{el}^{th}/E_c$  with  $W_{el}^{th}$  in equation (23) for an elastic impact i.e., with  $C_{plate} = 1.21$ . The red full line is the energy ratio  $W_{el}^{th'}/E_c$  corrected with  $C_{plate}$  dependence on parameter  $\lambda_Z$ , the blue line is the viscoelastic energy ratio  $W_{visc}/E_c$  [equation (35)] and the thick green line is the theoretical lost energy ratio, which is the sum of  $W_{el}^{th'}/E_c$  and  $W_{visc}/E_c$ .



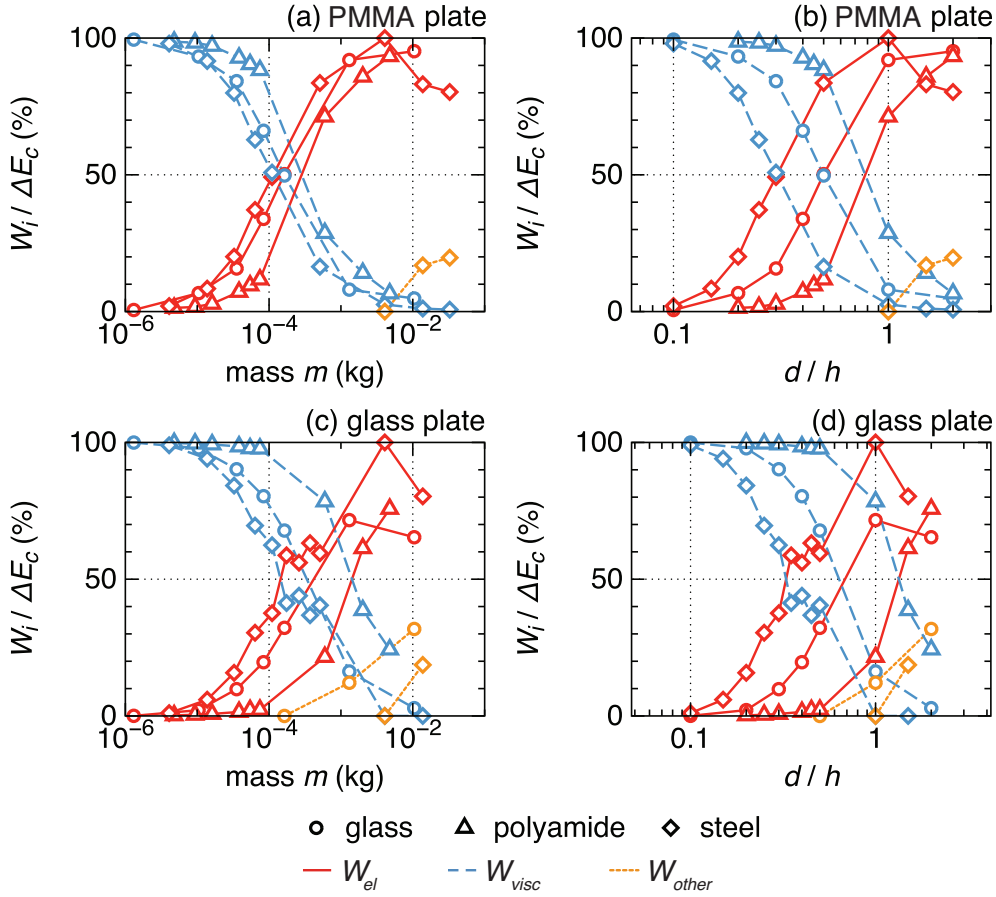


**Figure 12.** Percentage of the total energy lost in elastic waves  $W_{el}/\Delta E_c$  (red full line), by viscoelastic dissipation  $W_{visc}/\Delta E_c$  (blue dashed line) and by other processes  $W_{other}/\Delta E_c$  (orange dotted line) as a function of (a)-(c) the bead mass  $m$  and (b)-(d) the ratio of the bead diameter  $d$  over the plate thickness  $h$  for impacts of glass (circles), polyamide (triangles) and steel (diamonds) beads dropped from height  $H = 10$  cm on (a)-(b) the PMMA plate and on (c)-(d) the glass plate.

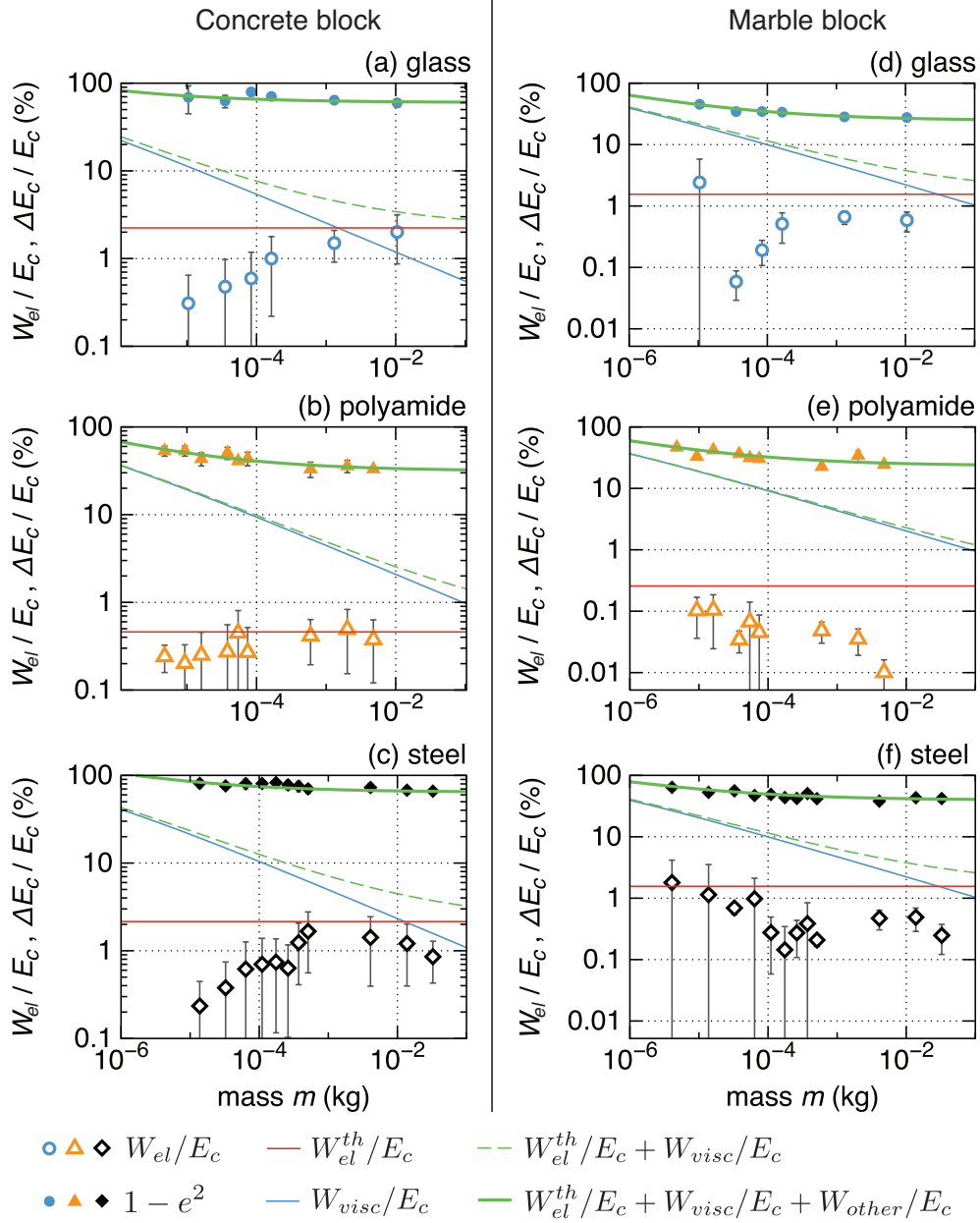


**Figure 13.** Ratio of the measured radiated elastic energy  $W_{el}$  over the impact energy  $E_c = \frac{1}{2}mV_z^2$  (empty symbols) and measured lost energy ratio  $\Delta E_c/E_c = 1 - e^2$  (full symbols) as a function of bead mass  $m$  for impacts of (a)-(d) glass, (b)-(e) polyamide and (c)-(f) steel beads on (a) to (c) the concrete block and on (d) to (f) the marble block. The red line represents the theoretical ratio  $W_{el}^{th}/E_c$  with  $W_{el}^{th}$  in equation (24) with  $C_{block} = 0.02$ . The blue line is the viscoelastic energy ratio  $W_{visc}/E_c$  [equation (35)]. The dashed green line is the theoretical lost energy ratio  $W_{el}^{th}/E_c + W_{visc}/E_c$ . The thick green line is the same ratio plus the percentage  $W_{other}/E_c$  of energy lost in other processes, which is assumed independent of the bead mass  $m$  (see text).

D R A F T
September 11, 2015, 6:01pm
D R A F T

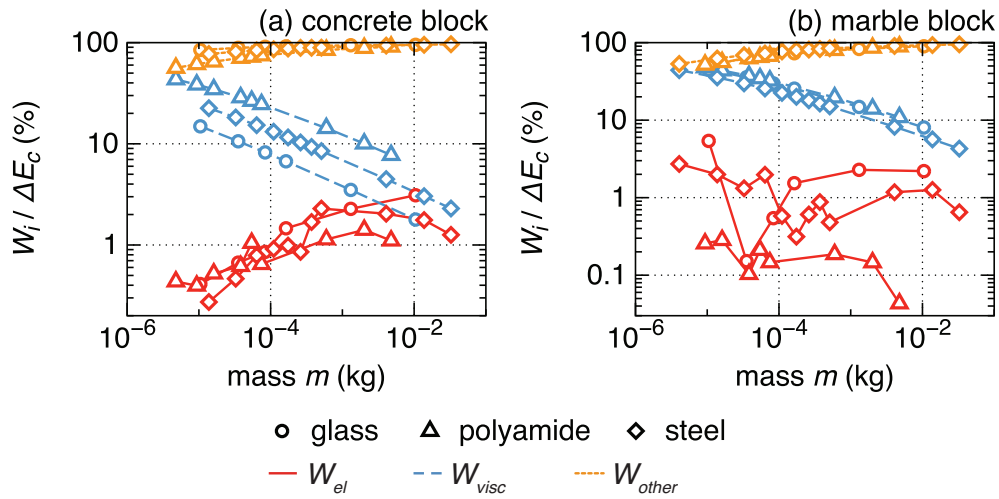


**Figure 14.** Percentage of the total energy lost in elastic waves  $W_{el}/\Delta E_c$  (red full line), by viscoelastic dissipation  $W_{visc}/\Delta E_c$  (blue dashed line) and by other processes  $W_{other}/\Delta E_c$  (orange dotted line) as a function of the bead mass  $m$  for impacts of glass (circles), polyamide (triangles) and steel (diamonds) beads dropped from height  $H = 10$  cm on (a) the concrete block and on (b) the marble block.

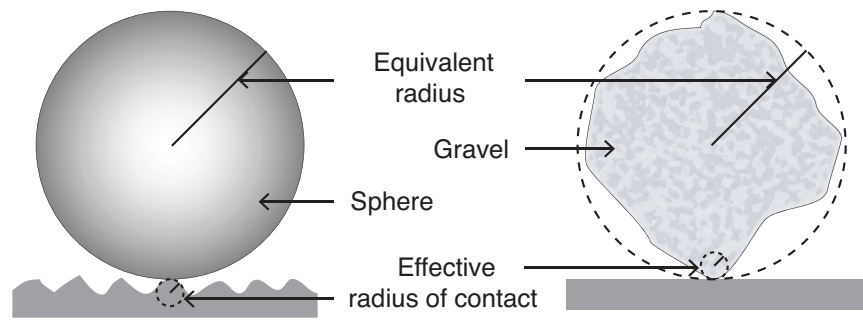


**Figure 15.** Schematic of the contacts between a sphere and a rough surface and between a rough gravel and a flat surface.

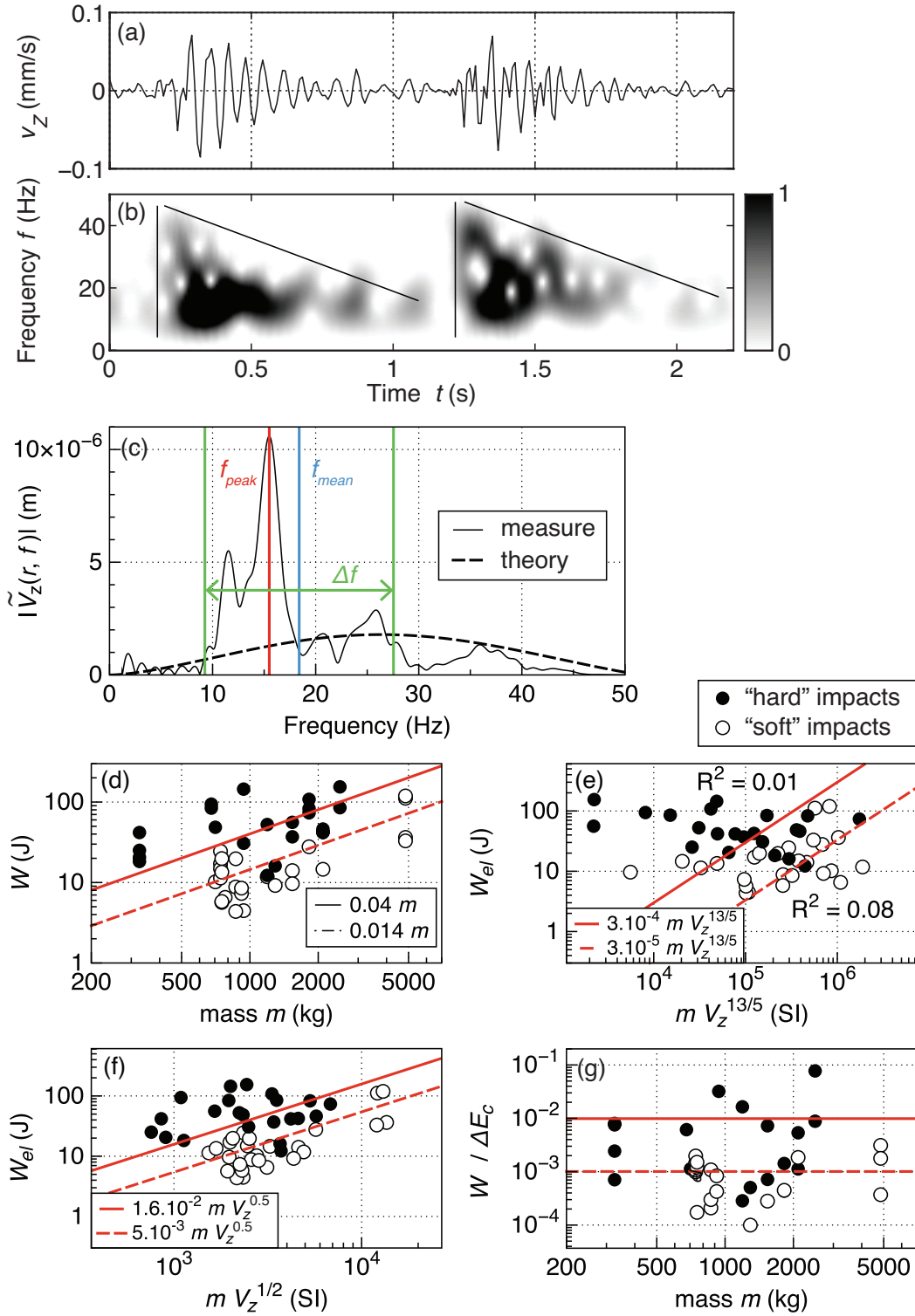


**Figure 16.** (a) Vertical vibration speed  $v_z(r, t)$  generated by two successive impacts of a boulder of mass  $m = 326$  kg on the rock slope. (b) Spectrogram of the signal in (a). Darker shape represents higher energy (normalized). The black lines highlight the triangular shape of the spectrograms. (c) Amplitude spectrum  $|\tilde{V}_z(r, f)|$  for the first impact, with the peak  $f_{peak}$  and mean  $f_{mean}$  frequencies and the synthetic spectrum computed with the convolution of *Hertz* [1882]’s force of elastic impact with the Green’s function of Rayleigh waves. (d) to (f) Radiated elastic energy  $W_{el}$  for different boulders documented in Tahiti as a function of (d) the mass  $m$  and of parameters (e)  $mV_z^{13/5}$  and (f)  $mV_z^{0.5}$ , with associated

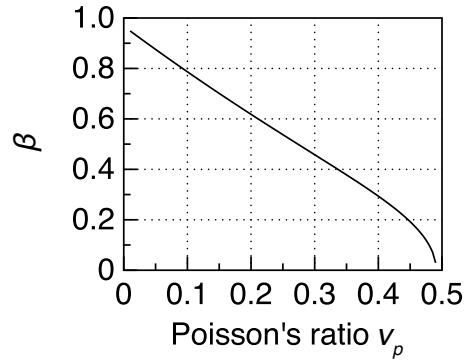


**Figure 17.** Coefficient  $\beta$  defined by equation (A7) as a function of the Poisson ratio  $\nu_p$ .

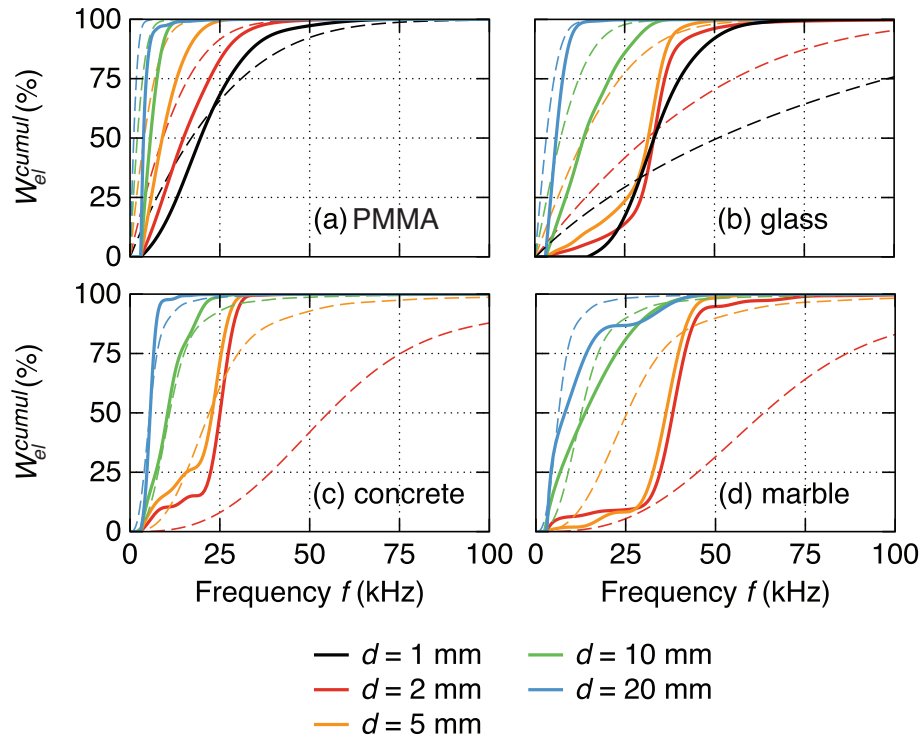


**Figure 18.** Cumulated radiated elastic energy  $W_{el}^{cumul}$  for the impact of steel beads of different diameters  $d$  (different colors) on (a) the PMMA plate, (b) the glass plate, (c) the concrete block and (d) the marble block, as a function of frequency  $f$ . Full line: experiments, dashed line: synthetics obtained with the convolution of the Green function with *Hertz* [1882]’s force of elastic impact.

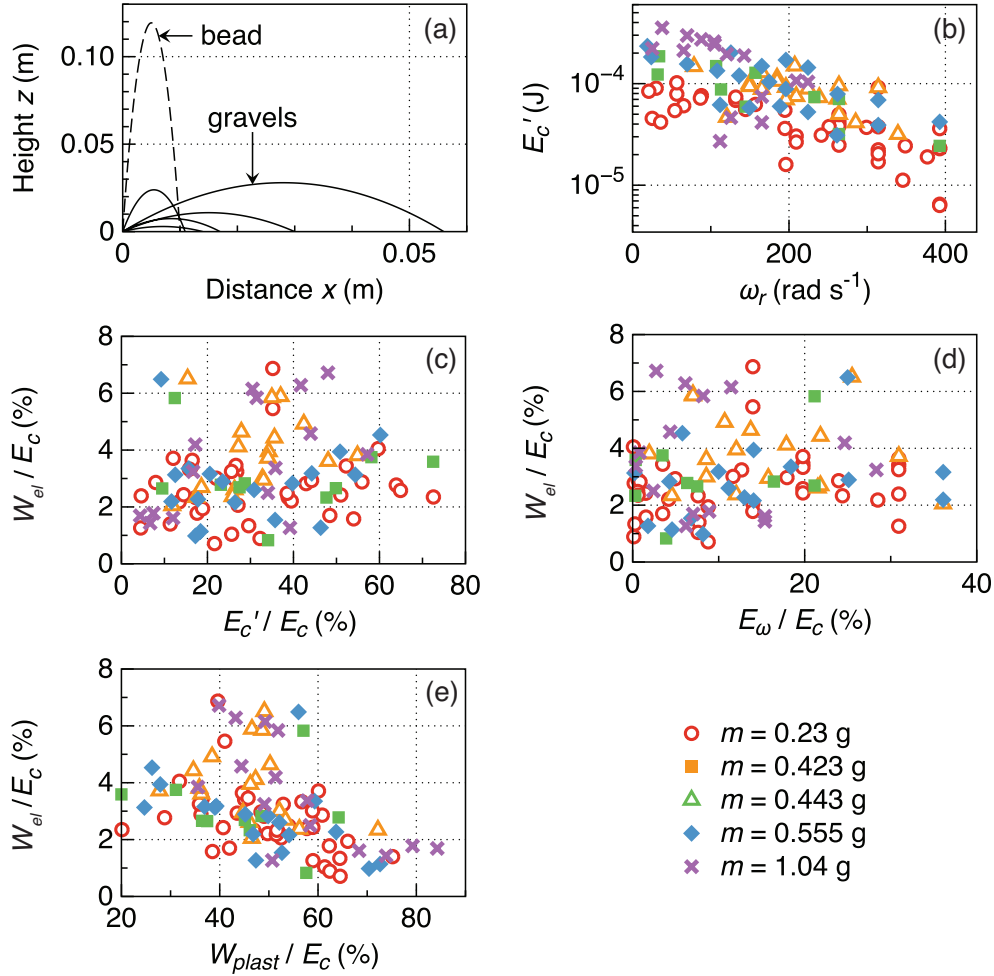


**Figure 19.** (a) Different rebound trajectories followed by the same gravel of mass  $m = 0.23$  g dropped from height  $H = 10$  cm several times on the glass plate (full lines) and one rebound trajectory followed a spherical bead of diameter  $d = 4$  mm dropped from the same height  $H$  (dashed line). Gravels of different masses  $m$  (different symbols) are dropped without initial spin from height  $H = 10$  cm on the glass plate. (b) Translational kinetic energy  $E'_c$  of the gravels after rebound as a function of their rotation speed  $\omega_r$  after rebound. (c) to (e) Percentage of impact energy lost in elastic waves  $W_{el}/E_c$  as a function of the percentage of the impact energy  $E_c$  converted (c) in rebound translational energy  $E'_c$ , (d) in rotational energy  $E_\omega$  and (e) in plastic deformation  $W_{plast}$ .

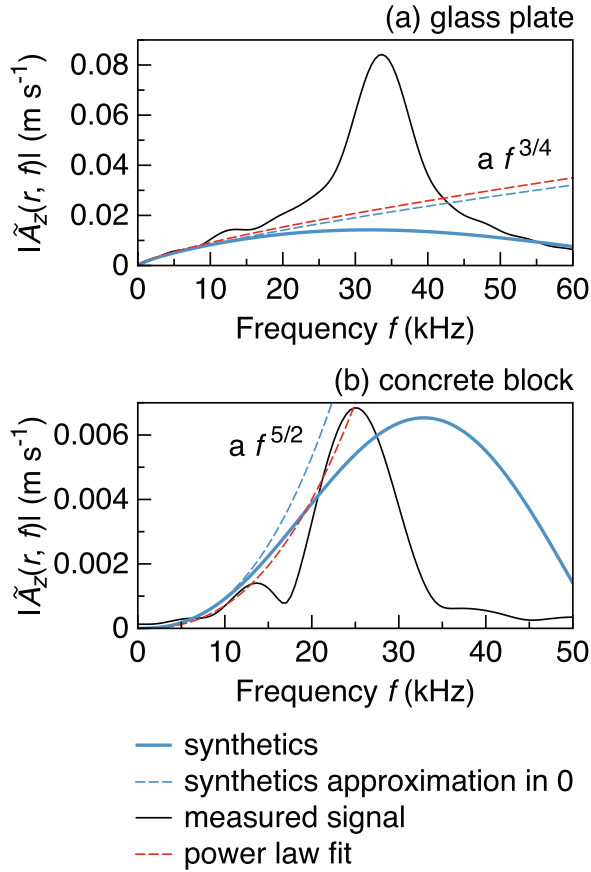


**Figure 20.** Measured amplitude spectrum  $|\tilde{A}_z(r, f)|$  (black line) and synthetic spectrum (thick blue line) for the impact of a steel bead of diameter 5 mm on (a) the glass plate and (b) the concrete block. The blue dashed line is the power law approximation for low frequencies of the synthetic spectrum. The red dashed line is an adjustment of the low frequencies content of the measured spectrum with the power law.